

Effect of climate warming on the timing of autumn leaf senescence reverses at the summer solstice

Constantin Zohner (✉ constantin.zohner@gmail.com)

ETH Zurich <https://orcid.org/0000-0002-8302-4854>

Leila Mirzagholi

ETH Zurich

Susanne Renner

Washington University

Lidong Mo

ETH Zurich <https://orcid.org/0000-0003-3805-7638>

Raymo Bucher

ETH Zurich

Daniel Palouš

Charles University in Prague

Yann Vitasse

University of Neuchâtel <https://orcid.org/0000-0002-7454-505X>

Yongshuo Fu

Beijing Normal University

Benjamin Stocker

ETH

Thomas Crowther

Swiss Federal Institute of Technology in Zurich <https://orcid.org/0000-0001-5674-8913>

Biological Sciences - Article

Keywords: Plant growth, Senescence, Phenology, Global warming, Climate change, Carbon cycle

Posted Date: February 9th, 2022

DOI: <https://doi.org/10.21203/rs.3.rs-1336514/v1>

License:  This work is licensed under a Creative Commons Attribution 4.0 International License.

[Read Full License](#)

1 **Effect of climate warming on the timing of autumn leaf senescence reverses**
2 **at the summer solstice**

3
4
5
6
7
8
9 Constantin M. Zohner^{1*}, Leila Mirzagholi¹, Susanne S. Renner², Lidong Mo¹, Raymo Bucher¹, Daniel
10 Palouš^{1,3}, Yann Vittasse⁴, Yongshuo H. Fu⁵, Benjamin D. Stocker⁶, Thomas W. Crowther¹

11
12 ¹Institute of Integrative Biology, ETH Zurich (Swiss Federal Institute of Technology), Universitätsstrasse 16,
13 8092 Zurich, Switzerland; ²Department of Biology, Washington University, Saint Louis, MO 63130, United
14 States; ³Department of Experimental Plant Biology, Charles University in Prague, Viničná 5, CZ 128 44,
15 Czech Republic; ⁴WSL Swiss Federal Institute for Forest, Snow and Landscape Research, Birmensdorf,
16 Switzerland; ⁵College of Water Sciences, Beijing Normal University, Beijing, China; ⁶Department of
17 Environmental Systems Science, Institute of Agricultural Sciences, ETH Zurich, Switzerland.

18
19
20 *Author for correspondence: Constantin Zohner, constantin.zohner@gmail.com

21
22 **Keywords:**
23 Plant growth | Senescence | Phenology | Global warming | Climate change | Carbon cycle
24

25 **Abstract**
26 Climate change is causing shifts in the growing seasons of plants^{1,2}, affecting species performance and
27 interactions^{3,4} as well as global carbon, water and nutrient cycles^{5,6}. How the timing of autumn leaf
28 senescence in extra-tropical forests will change remains unclear because of the complex seasonal
29 interaction of climate warming, earlier and enhanced vegetation activity, and the annual day-length cycle^{7–}
30 ¹⁰. Here we use experiments, long-term ground observations, and satellite-based vegetation monitoring to
31 show that early-season and late-season warming have opposite effects on the onset and progression of
32 leaf senescence, with a reversal occurring at the year's longest day (summer solstice). Across ~84% of the
33 northern forest area, increased temperature and vegetation activity before the solstice led to an earlier
34 senescence onset (10% greenness loss) of, on average, -1.6 ± 0.1 days-per-°C, while warmer post-solstice
35 temperatures did not affect senescence onset but reduced its speed (progression to 50% greenness loss)
36 by 0.8 ± 0.1 days-per-°C. Due to the earlier senescence onset, the day at which autumn temperature starts
37 driving senescence progression has been shifting to ever earlier dates, between 1951–2015 at a rate of -0.20 ± 0.07 days per year. These developmental constraints suggest that senescence will start earlier but
38 progress more slowly in the future, revealing Northern Hemisphere-wide compensation effects on trends in
39 growing-season length, caused by enhanced pre-solstice vegetation activity. This new mechanistic insight
40 improves our ability to model carbon uptake by extra-tropical forests under climate change.
41

42
43
44
45 **Main text**
46 The phenological cycles of trees exert a strong control on the structure and functioning of ecosystems^{4,11}
47 and global carbon, water and nutrient cycles^{2,5,6}. Anthropogenic climate change has resulted in shifts in the
48 growing seasons of temperate and boreal trees, with the start of the season today occurring, on average,
49 two weeks earlier than it did during the 19th and 20th century¹² and the end of the season (EOS) being
50 delayed^{1,6,13}. Each day of a longer growing season may increase net ecosystem carbon uptake by 3.0–9.8
51 gC m⁻² (ref⁶). Yet, due to the complex and interactive effects of growing-season climate and the annual day-
52 length cycle the direction of EOS changes in response to climate change has remained highly
53 uncertain^{8,9,14,15}.

54 Characterizing the interplay among the environmental drivers of EOS is integral to improving our
55 understanding of vegetation development and tree growth. A key outstanding question is how day length
56 and climate effects interact and vary throughout the growing season. Local observations and experiments
57 have shown that early-season warming, causing earlier spring leaf-out and faster development, tends to
58 advance EOS dates^{8–10,16}, whereas late-season warming has the opposite effect, delaying the EOS^{17,18}.
59 Accelerated development and increased vegetation activity in the beginning of the season might drive earlier
60 autumn senescence through a variety of possible mechanisms, such as developmental and nutrient
61 constraints^{9,19}, seasonal built-up of water stress^{20,21}, or radiation-induced leaf ageing²². In contrast, later on
62 in the season, a direct effect of temperature (cooling) is likely to dominate phenological responses^{14,23,24}. If
63 these trends are correct, then climate warming has opposing effects at the start and end of the growing
64 season, with a reversal of effects somewhere in between. Yet, we lack a global understanding of the
65 seasonal effects of plant growth and climate on autumn phenology, limiting our ability to forecast future
66 growing seasons and carbon uptake in extra-tropical forests.

67 Here we test whether early-season vegetation activity and development drive an earlier EOS across
68 northern forests, with day length providing the linkage between seasonal activity, air temperature warming,
69 and autumn phenology (Fig. 1). Cell division, tissue formation, and growth in northern trees are highest at
70 the beginning of the season and decline with shortening days^{25–28}, the adaptive reason being the limited
71 time remaining for tissue maturation and bud set before the first frost²⁹. We thus expected that inter-annual
72 variation in EOS timing is a function of early-season growth, with an earlier onset of senescence in warm,
73 high-activity years than in cold, low-activity years (Fig. 1 scenario 1 *versus* 2). Once EOS has begun, its
74 progression (towards full dormancy) should be modulated by autumn temperature, with faster chlorophyll
75 breakdown in colder autumns than in warmer autumns²⁴ (Fig. 1 scenario A *versus* B). If early-season
76 development continues to accelerate due to advances in leaf-out timing and higher air temperature^{2,6,30,31},
77 this might cause an ever earlier EOS onset, eventually outweighing the delay in the progression of
78 senescence due to warmer autumns.

To test these hypotheses, we combined phenology data from i) satellite observations across Northern Hemisphere temperate and boreal forests, ii) ground-sourced European observations from widespread deciduous trees³², and iii) controlled experiments on European beech. As a proxy for vegetation activity, we used three photosynthesis models (satellite-derived gross-primary productivity [GPP]³³, LPJ⁹ and p model³⁴). We then ran linear models to test for the monthly and seasonal effects of photosynthesis, temperature, short-wave radiation and water availability on EOS dates. The satellite data allowed us to differentiate between the onset of senescence and its progression, by analysing the dates when greenness had dropped by 10% (EOS_{10}) or 50% (EOS_{50}) relative to the seasonal maximum. The experiments allowed us to directly test for seasonal variation in the effects of day length, air temperature, radiation, water, and nutrient availability. Finally, we mapped the relative effects of early-season vegetation activity and late-season climate across Northern Hemisphere temperate and boreal forests to test for possible historic-biogeographic patterns in the drivers of autumn senescence.

Satellite-based phenology data (Fig. 2), European plot data (Fig. 3), and experiments (Fig. 4) all revealed a consistent advancing effect of pre-solstice (i.e., pre-21 June) vegetation activity on EOS dates, which declined after the June solstice. Thus, across ~84% of the northern forest area (32% or 22% with $p < 0.1$ or < 0.05), increased pre-solstice photosynthesis and temperature led to an earlier onset of senescence (Fig. 2a,c and Extended Data Fig. 1a,c), with each 10% increase in photosynthesis and each 1°C increase in temperature on average resulting in -2.8 ± 0.1 and -1.6 ± 0.1 days earlier EOS_{10} , respectively (Fig. 2i and Extended Data Fig. 1i). The advancing effect of pre-solstice vegetation activity was most pronounced at mid-latitudes (45–60°N) and decreased toward lower latitudes (Fig. 2b). A significant delaying effect of pre-solstice activity was found for fewer than 1% of pixels (Fig. 2d,e). Increased post-solstice photosynthesis and temperature, by contrast, had a much smaller effect on the onset of senescence (EOS_{10} dates; Figs. 2f-h and 5a and Extended Data Fig. 1f-h) but slowed down its progression (EOS_{50} dates) by, on average, 0.8 ± 0.1 days per °C (see Figs. 5b and Extended Data Fig. 2 for satellite observations and Figs. 3 and 5c for European plots). Precipitation and CO₂ levels had comparatively small effects (Fig. 2f).

The reversal at the summer solstice of the effects that air temperature and vegetation activity have on EOS dates was consistent across i) both EOS metrics used here, i.e., the onset of senescence (EOS_{10} ; Extended Data Fig. 1) and its progression (EOS_{50} ; Extended Data Fig. 2), ii) forest types (Fig. 2a and Extended Data Fig. 3), and iii) a set of alternative variables linked to growing-season activity and development, namely climate-derived productivity (Figs. S1 and S2), day-time temperature (T_{day} ; Extended Data Figs. 1 and 2), and short-wave radiation (Figs. S3 and S4). The effect reversal at the June solstice was further supported by an analysis that used 10-day moving steps around the solstice (Fig. 2h). Furthermore, along the full latitudinal gradient (30°N–65°N) studied here, the early-season period during which vegetation activity exhibited an advancing effect on EOS_{10} dates consistently ended right after the solstice at June ~26 (Extended Data Fig. 4).

Our finding that the onset of senescence is driven by pre-solstice activity and development, while its rapid or slow progression depends on autumn temperature (Fig. 5b,c and Extended Data Fig. 2) suggests that, under global warming, senescence will start earlier but progress more slowly (scenario 2B in Fig. 1). Indeed, analysis of the temporal trends in remotely-sensed EOS dates and pre-solstice vegetation activity showed that across all analysed northern forest pixels, the onset of senescence (EOS_{10} date) has advanced by an average of -0.4 ± 0.1 days per decade between 2001–2018 (Fig. 2j), in parallel with increased pre-solstice vegetation activity (Extended Data Fig. 5a-b), with the strongest advances in EOS_{10} dates found for regions with the largest increase in pre-solstice GPP (Extended Data Fig. 5k). By contrast, senescence progression (EOS_{50} date) has slowed by an average of 1.5 ± 0.1 days per decade (Extended Data Fig. 2l), in parallel with warmer autumns (Extended Data Fig. 5i,j), with the largest extension of the overall senescence duration found for regions with the largest increases in autumn temperature (Extended Data Fig. 5m). When removing the effect of pre-solstice photosynthesis (Fig. 2i) by including it as a fixed effect in addition to year, the model predicted delays in EOS_{10} and EOS_{50} dates of $+1.3 \pm 0.1$ and $+2.0 \pm 0.1$ days per decade, respectively (Figs. 2k and S2m), underscoring the strong advancing effect of the ongoing acceleration in pre-solstice vegetation activity on temporal trends in leaf senescence.

In line with the satellite observations, high pre-solstice vegetation activity also correlated with advanced EOS_{50} dates in the European plot data, across all four species (Fig. 3b) and across a set of alternative variables (LPJ model-derived photosynthesis [Fig. 3], P-model-derived photosynthesis [Fig. S5], day-time temperature [T_{day} ; Fig. S6], and cumulative short-wave radiation [Fig. S7]. Based on these findings,

we ran multivariate mixed models, including or excluding the effects of pre-solstice or post-solstice (solstice to mean EOS₅₀) activity and precipitation to determine the relative importance of seasonal activity, precipitation, CO₂ levels, and autumn night-time temperature (Autumn T_{night}). Pre-solstice activity and autumn T_{night} had the strongest effects on EOS₅₀ dates, with the effect of pre-solstice photosynthesis being ~3 times greater than that of precipitation and atmospheric CO₂ (Fig. 3h). EOS predictions from these models show that the model representing both pre- and post-solstice effects adequately captures within-site EOS₅₀ trends in response to mean annual temperature (advance of -0.4 days per each °C increase in mean annual temperature, Fig. 3g). In contrast, the post-solstice model representing only post-solstice activity and precipitation, predicts delays of +0.8 days per °C, while the pre-solstice model predicts advances of -1.0 days per °C, demonstrating that information on both pre- and post-solstice climate is necessary to reproduce the observed EOS₅₀ responses to rising temperature.

The offsetting effect of pre-solstice development on autumn-warming-induced delays in EOS₅₀ also is apparent when quantifying either regional trends over the past 70 years (time series and species as random effects; Fig. S8) or spatial patterns in EOS₅₀ (year and species as random effects; Fig. S9). On average, European EOS₅₀ dates have been delayed by only +0.35 ± 0.02 days per decade (Fig. S8b). Yet, when keeping pre-solstice productivity constant by including it as a fixed effect in addition to year, the model predicts a delay of +0.81 ± 0.03 days per decade (Fig. S8d), showing that the increase in pre-solstice vegetation activity has offset up to ~60% of the delay in EOS₅₀ that would have occurred if pre-solstice productivity had not increased. This explains why EOS₅₀ delays have contributed only ~15% (2.4 ± 0.2 days) to the 16.7 ± 0.4 day-long extension of the growing season that has occurred over the past 70 years (Fig. S8a, b). The advancing effect of pre-solstice productivity on EOS dates is also evident across spatial gradients (Fig. S9 a,c), such that EOS₅₀ dates occur only +0.85 ± 0.03 days later for each 1°C increase in that region's autumn temperature, while they occur +1.40 ± 0.04 days °C⁻¹ later if the advancing effect of pre-solstice productivity is removed (39% reduction of the geographic autumn temperature response; Fig. S9 b,d).

The progression of senescence is modulated by autumn air temperature, as is evident from the delaying effect of warm autumns on EOS₅₀ dates (Figs. 2, 3 and 5 and Extended Data Fig. 6b,c). However, if increased pre-solstice vegetation activity and development (Extended Data Fig. 5a–b) indeed is the main driver of an earlier onset of EOS, one should find an ever earlier susceptibility of trees to autumn cooling. To test this, we conducted temporal moving-window analyses on the European long-term observations showing whether the reversal date – at which increased productivity and temperature start to be associated with delayed EOS₅₀ dates – has shifted over recent decades. The results reveal that this is the case, with reversal dates shifting to earlier dates by an average of -0.6 to -1.0 days per year (Fig. 3f and Figs. S5f–S7f or Fig. S10b for a shorter moving window). It is also reflected in the moving windows of monthly effect sizes, which show that July photosynthesis, temperature and radiation have been more strongly associated with delayed EOS₅₀ dates over recent decades (Fig. 3c and Figs. S5c–S7c). As an alternative method of determining when autumn cooling starts driving senescence progression, we modelled the autumn period best explaining EOS₅₀ dates and found that it has advanced by -0.20 ± 0.07 days per year for the 1966–2015 period (Extended Data Fig. 7a) or by -0.43 ± 0.09 days per year for the 1981–2015 period (Extended Data Fig. 7b). This earlier start of the period when trees react to autumn cooling provides further evidence for an earlier onset of senescence in response to increased early-season development.

Previous research has suggested a negative feedback between growing-season activity and autumn phenology, with increased activity driving earlier EOS⁹. These findings came from monitoring of European deciduous trees and neglected possible mediating effects of the annual day length cycle. The satellite data analysed here now reveal such negative feedback across the entire Northern Hemisphere temperate and boreal forest biome, implying a widespread constraint on future growing-season extensions in response to global warming. To disentangle the environmental drivers of this negative feedback, we ran univariate (Extended Data Fig. 8) and multiple linear regression models that included air temperature, solar radiation, and water availability in addition to spring budburst dates as predictor variables, all of which factors have been shown to affect leaf senescence dates^{8–10,21,35–37} (Fig. 5 and Extended Data Fig. 9 or Fig. S11 using soil moisture instead of precipitation to represent water availability). The results showed that leaf-out timing, cumulative radiation, and water availability had small effects on EOS₁₀ and EOS₅₀ dates (Fig. 5), suggesting that temperature-driven development and growth, rather than a constrained leaf lifespan,

186 radiation-induced leaf ageing, or drought effects, is driving the advancing effect of early-season vegetation
187 activity on autumn phenology.

188 To further isolate the mechanisms driving the discovered reversal of the effects of global warming
189 around the June solstice, we designed two experiments using a dominant European tree (*Fagus sylvatica*).
190 In a first experiment, we cooled (day- / night-time temperature = 10°C / 5°C) and shaded (~84% light
191 reduction) saplings during different times of the season. Pre-solstice temperature again had a strong
192 advancing effect on autumn phenology, with cooling of trees in June causing a delay in EOS₁₀ and EOS₅₀
193 dates of +16.5 ± 6.6 days and +10.2 ± 2.5 days (mean ± standard error), respectively, whereas cooling in
194 July had no effect and August cooling tended to advance EOS dates (Fig. 4a and S12a), in full agreement
195 with the global-scale remote sensing data and the European ground observations. The effect of shading
196 was small before the June solstice and most pronounced during July – the month with the highest mean
197 daily radiation and temperature – with +6.5 ± 2.8 days later EOS₅₀ under shade conditions. Radiation effects
198 thus followed a different seasonal pattern than temperature, supporting a direct effect of radiation on leaf
199 ageing^{22,36}. Summer photosynthesis was equally reduced in both the shade and the temperature treatments
200 by 52–72% compared to the control (Fig. S13). That pre-solstice temperature, but not pre-solstice light
201 availability, affected EOS dates provides further support for the idea that accelerated growth and
202 development under warmer temperatures, rather than photosynthesis- or UV-induced leaf ageing, are the
203 main drivers of the pre-solstice effects on senescence dates.

204 In a second experiment, we tested the effects of elevated sink strength (nutrient addition) and soil
205 moisture. In agreement with the idea that nitrogen supply governs the sink control of leaf development and
206 senescence¹⁹, there was a strong delaying effect of extra nutrients on EOS dates, with +22 ± 6-day (mean
207 ± standard error) later EOS₁₀ and +14 ± 5-day later EOS₅₀ in trees grown in nutrient-rich soils compared to
208 trees grown in NPK-poor soils (Extended Data Fig. 10 and Fig. S14). Reduced soil moisture slightly delayed
209 EOS dates (by ~2 days) up to a threshold at which complete soil dehydration led to premature leaf die-off
210 (Extended Data Fig. 10 and Fig. S15). These experimental findings match our findings from European
211 phenological gardens and satellite-derived *in situ* observations, in which direct precipitation or soil moisture
212 had smaller effects than air temperature and early-season growth.

213 In conclusion, our Northern-Hemisphere-wide investigation of the seasonal drivers of autumn
214 phenology shows a consistent reversal in the effects of global warming on leaf senescence timing after the
215 summer solstice, present i) across large biogeographic ranges with varying pre-solstice growth (satellite
216 data), ii) in four tree species with different spring phenologies (ground data), and iii) under controlled
217 experimental conditions. These findings lend strong support to the idea that the annual day-length cycle
218 mediates the seasonal control on EOS by vegetation activity and air temperature (Solstice-as-Phenology-
219 Switch [SPS] hypothesis; Fig. 1). Hence, EOS variations emerge as the result of a complex synchronization
220 between a trees' developmental state, seasonal variation in the circadian rhythm and climate fluctuations.
221 This mediation provides a unifying framework to explain previous results on the seasonal effects of
222 temperature on autumn phenology, in which the magnitude and direction of the temperature effect varied
223 depending on the season^{15,17,18,31,38,39}. Across the whole temperate and boreal forest area, warmer pre-
224 solstice temperatures drive an earlier onset of senescence, while warmer post-solstice temperatures slow
225 down the progression of senescence, suggesting that senescence will start earlier but progress more slowly
226 in the future.

227 The reversal in how trees respond to temperature during the summer likely evolved as an adaptation
228 to seasonal climates with harsh winters because it allows plants to reliably predict the progression of the
229 seasons and prepare for winter dormancy long before the temperature actually starts dropping²⁹. A response
230 shift around the June solstice enables trees to initiate tissue maturation and the physiological processes of
231 leaf senescence and nutrient resorption²⁶ in a fine-tuned balance between source and sink dynamics. Trees'
232 physiological response to the annual day length cycle essentially calibrates their seasonal rhythms and
233 mediates how they react to warm or cool temperatures, now and in the future. Improved models of plant
234 development and growth under climate change will need to incorporate the reversal of warming effects
235 around the summer solstice.

236

237 **Methods**
238239 **Analysis of ground-sourced European phenology observations**
240241 **Phenology data.** Direct observations of spring leaf-out and autumn leaf senescence dates for four dominant
242 tree species from 1951–2015 were collected from the Pan European Phenology Project (www.pep725.eu)³²,
243 which provides open-access phenological data for Europe (mainly Germany, Switzerland, and Austria; Fig.
244 S16). The start-of-season (SOS) was defined as the date when the first leaf stalks are visible (BBCH11).
245 For a few time series, BBCH11 data was not available, and we used the date when 50% of leaf stalks are
246 visible (BBCH13) instead. The end-of-season (EOS₅₀) corresponded to the date when 50% of leaves had
247 lost their green color (BBCH94). Alternatively, for time series for which BBCH94 data was not available, we
248 used the date when 50% of leaves had fallen (BBCH95).
249250 **Data cleaning.** Following ref⁴⁰, we removed (i) individual time series with fewer than 15 years of leaf-out
251 and leaf senescence observations, (ii) dates deviating from an individual's median more than 4 times the
252 median absolute deviation, and (iii) time series for which the standard deviation of phenological observations
253 across years was higher than 20 for leaf-out and 25 for leaf senescence. The thresholds differed because
254 the mean absolute deviation for leaf-out time series was lower than that for leaf senescence. In total, we
255 kept records of the four most abundant tree species in the database (*Aesculus hippocastanum*, *Betula*
256 *pendula*, *Fagus sylvatica*, and *Quercus robur*) at 3,851 sites across Central Europe, resulting in a total of
257 396,411 phenological observations (individuals x year) and 12,759 individual time series (with a median
258 length of 33 years; minimally 15 years, maximally 65 years) during the period 1951–2015 (Fig. S16). The
259 number of time series per species was 3,477 for *Aesculus hippocastanum*, 3,375 for *Betula pendula*, 3,050
260 for *Fagus sylvatica*, and 2,857 for *Quercus robur*.
261262 **Climate data.** For each site, information on air temperature, precipitation, air humidity, net and downward
263 short-wave radiation, net long-wave radiation, and soil moisture (at 0–10 cm and 10–40 cm depth) at a
264 spatial resolution of 0.25 arc degrees (approximately 25 km at the equator) and a cadence of 3 hours were
265 derived from the Global Land Data Assimilation System (GLDAS)⁴¹ for the period 1951–2015. We then
266 calculated daily means for each of the climate variables and the day-time (T_{day}) or night-time (T_{night})
267 temperature. To obtain T_{day} and T_{night} , we approximated hourly temperatures using the “stack_hourly_temps”
268 R function from the chillR package⁴², and then calculated the means of all temperatures from sunrise to
269 sunset or sunset to sunrise, respectively, whereby sunset and sunrise were calculated with the “daylength”
270 function (chillR package) based on latitude and day-of-year information. Means of monthly atmospheric CO₂
271 concentrations for each degree of latitude were taken from the CMIP6 concentration dataset⁴³. To represent
272 soil water availability in the photosynthesis model (see next section), for each site, we extracted physical
273 soil properties (clay and coarse fragment content) from world maps at 250 m spatial resolution through
274 SoilGrids⁴⁴. Soil texture was computed based on the texture-to-parameter conversion by ref⁴⁵, using the
275 Database of Hydraulic Properties of European Soils (HYPRES) implemented in the R package soiltexture⁴⁶.
276277 **Photosynthesis calculation.** We derived daily net daytime photosynthesis estimates (excluding night-time
278 respiration) [Anet_{day}] from two photosynthesis models, hereafter referred to as LPJ model and P model.
279280 *LPJ model:* Anet_{day} was computed using empirical information on T_{day} , minimum and maximum daily
281 temperature, air humidity, atmospheric CO₂, short- and long-wave radiation, and soil moisture, following the
282 coupled photosynthesis and stomatal conductance sub-model of LPJ-GUESS⁴⁷. The temperature response
283 of photosynthesis followed ref⁴⁸, with the minimum temperature limit at 1°C, the maximum at 45°C, and the
284 temperature optimum between 18°C and 25°C (see Fig. S17). To account for the effect of water availability
285 on photosynthesis⁴⁹, we included a daily water stress factor in our seasonal photosynthesis estimates, which
286 was calculated following the water balance module of LPJ-GUESS⁵⁰. The fraction of absorbed
287 photosynthetically active radiation (fAPAR) was set to 0 before SOS and to 0.5 after the SOS date, since
288 nearly half of the short-wave radiation is intercepted by the canopy⁴⁵. See Supplementary Materials in Zani
289 et al.⁹ for a detailed description of the model and [Github](#) for the annotated R code.
290290 *P model* (developed by Stocker et al.³⁴ and following the theory of refs^{51,52}): Photosynthesis was computed
as a function of T_{day} , vapor pressure deficit, atmospheric CO₂, short-wave radiation, and relative soil

moisture (actual moisture relative to field capacity). In addition, information on elevation and the site-level ratio of actual over potential annual mean evapotranspiration was included to represent atmospheric pressure and average local aridity, respectively. Apparent quantum yield efficiency was set to 0.087, optimal leaf-internal/ambient CO₂ ratios (ci/ca) were calculated based on the method developed in ref⁵¹, and limitations in the photosynthetic capacity for electron transport (Jmax) were accounted for based on the method developed in ref⁵². As for the LPJ model, fAPAR was set to 0 before SOS. The P model was run via the rmodel function in the R package rmodel³⁴.

Analysis. In total, we included seven variables in our analyses: LPJ-model photosynthesis, P-model photosynthesis, T_{day} and T_{night}, short-wave radiation, CO₂ levels, and precipitation.

Seasonal and monthly photosynthesis/climate: To obtain monthly photosynthesis, T_{day}, and short-wave radiation values, we took the sums of daily photosynthesis and radiation values and the means of daily T_{day} values for each month (January to October) [see e.g., Fig. 3a, b]. Similarly, we aggregated values of these variables for six 30-day intervals before, during, and after the June solstice (with 10-day steps), i.e., from May 13 to June 11, May 23 to June 21, June 2 to July 1, June 12 to July 11, June 22 to July 21, and July 2 to July 31 (see e.g., Fig. 3d). In addition, we summed the daily photosynthesis values for eight periods (SOS to May 22, SOS to June 21 [solstice], SOS to July 21, SOS to August 20, SOS to mean EOS₅₀, May 22 to mean EOS₅₀, June 21 [solstice] to mean EOS₅₀, and July 21 to mean EOS₅₀) [see e.g., Fig. 3e]. For T_{day} and short-wave radiation we calculated the means for eight periods starting on 21 March instead of the variable SOS date.

Autumn temperature intervals: It is well known that cold temperatures at the end of the season accelerate the senescence process^{9,17,18}, and, for each time series, we therefore determined the optimal autumn interval for which temperature explains most of the variation in EOS₅₀ dates. To do so, we ran linear regressions between EOS₅₀ dates and the temperature interval (T_{day} or T_{night}) 10 to 120 days before the average EOS₅₀ date of each time series (with 10-day steps). Relationships were evaluated using both the coefficient of determination (R²) values and the standardized coefficients (Extended Data Fig. 6c). These analyses showed slightly higher R²s and standardized coefficients for T_{night} than for T_{day}, and, for each time series, we therefore included the respective T_{night} interval with the highest R² in the analyses (hereafter referred to as Autumn T_{night}, see e.g., Fig. 3h).

Models: To test for the effects of photosynthesis and climate parameters during different times of the year on EOS₅₀ dates, we ran linear mixed models, implemented in the R package lme4⁵³. All models included either both time series and species random effects, or only a time series random effect in case the model was run separately for each species. Both predictor and dependent variables were standardized – by subtracting the mean and dividing by the standard deviation – to obtain relative effect sizes. For the monthly models of photosynthesis, March to October values were included as predictors in the model, with March values representing the sum of January to March (Figs. 3 and S5). This aggregation was done because no or only very little photosynthesis occurred during the January-to-March period (average leaf-out date across all observations: 26 April). For the monthly T_{day} model, January to October values were included as predictors (Fig. S6a,b). To characterize the effects of photosynthesis, T_{day}, and short-wave radiation within 30-day-long intervals around the June solstice, we included the variable value within the respective interval and Autumn T_{night} (to control for autumn temperature) as fixed effects (Figs. 3d and S5d–S7d). To characterize the seasonal effects of photosynthesis, T_{day}, and short-wave radiation, we included the variable value within the respective interval as single fixed effect (Figs. 3e and S5e–S7e).

Finally, we ran mixed models based on the seasonal periods that emerged as the strongest drivers of leaf senescence, i.e., pre-solstice (leaf-out or March 21 to June 21) and post-solstice climate (June 22 to mean senescence date). Models were run separately for photosynthesis, T_{day} and short-wave radiation, and we accounted for possible effects of water availability, atmospheric CO₂ concentration, and autumn temperature by additionally including the sums of pre-solstice (March 20 to June 21) and post-solstice (June 21 to mean time series senescence date) precipitation, annual CO₂ concentration, and Autumn T_{night} as fixed effects (full model; Fig. 3g). To test for the individual effects of pre-solstice and post-solstice variables on model performance and predictions, we additionally ran models that only included either pre-solstice

photosynthesis, T_{day} , or radiation and pre-solstice precipitation (pre-solstice model) or post-solstice photosynthesis, T_{day} , or radiation and post-solstice precipitation (post-solstice model; Figs. 3g and S5g–S7g). To test for multicollinearity among covariates, we calculated variance-inflation factors – using the vif function implemented in the R package car⁵⁴, for all models that contained multiple variables, i.e., the monthly and the full models. All VIFs were < 2, indicating sufficient independence among predictors.

Moving-window analysis: To test whether the relative effects of variables have been changing over the past decades, we additionally ran all above-mentioned mixed models separately for each 20-year time period from 1966–2015. To ensure that the long-term average climate of sites did not differ across the moving-window periods as a result of site-level differences, we excluded high-elevation sites > 600 m a.s.l. as they were underrepresented in earlier years. We then tested whether the average long-term (1948–2015) climate of sites included in each moving-window period differed between years and found no trend (Fig. S18), demonstrating that there is no systematic bias in the average site-level climate conditions among moving windows. Within each 20-year moving-window, time series with fewer than 15 years of observations were excluded. To ensure that all sites were equally represented in each moving-window period, we ran a reduced analysis with 15-year moving-window intervals for the 1980–2015 period, including only time series for which at least 30 years of observations were available in total during 1980–2015 and for which at least 12 years were available during each 15-year moving window (Fig. S10).

To estimate the reversal date of the climate-autumn phenology relationship at which increased temperature and productivity start to be associated with delayed EOS₅₀ dates, we conducted moving-window analyses of the monthly photosynthesis/climate effects. To do so, for each 20-year (Fig. 3f) or 15-year (Fig. S10b) moving-window, we interpolated the date at which the effect of monthly photosynthesis/climate crosses the zero line during summer (see e.g., Fig. 3a). The dates were inferred both across species (based on models including time series and species random effects) and separately for each species (based on models including only time series random effects; see e.g., Fig. 3f). To estimate the overall trend in the reversal dates over time, we ran a linear regression between the reversal date obtained for each moving window and year.

As an alternative to estimating the day at which autumn temperature starts driving senescence progression, for each moving window, we estimated the autumn temperature-sensitive period, based on the autumn period for which temperature best explained variation in EOS₅₀ dates (see above paragraph on *Autumn temperature intervals*) [Extended Data Fig. 7].

Analysis of satellite-derived phenology observations

Phenology data. Spring leaf-out and autumn leaf senescence dates for the period 2001–2018 were collected from the MODIS Global Vegetation Phenology product (MCD12Q2 V6)⁵⁵, which provides phenological metrics at 500 m spatial resolution for every vegetated pixel on land derived from time series of the 2-band Enhanced Vegetation Index (EVI2) calculated from MODIS Nadir Bidirectional Reflectance Distribution Function (BRDF)-Adjusted Reflectance (NBAR). SOS was defined as the date when EVI2 first crossed 15% of the segment EVI2 amplitude greenness. EOS was defined as the date when EVI2 last dropped by 10% (EOS₁₀) or 50% (EOS₅₀) of the segment EVI2 amplitude, representing the start of senescence and mid-greendown, respectively.

Data cleaning. We extracted phenology information for all Northern Hemisphere pixels classified as mixed, broadleaf deciduous, evergreen needleleaf, or deciduous needleleaf forest (tree cover >60%) by the MODIS land cover type map (MCD12Q1 V6)⁵⁶. We removed pixels (i) for which phenology information for fewer than 15 years was available and (ii) for which the mean SOS occurred before March 1 or after May 31 and for which the mean EOS₅₀ occurred before July 18 and after November 30. We then aggregated the data to 0.25 arc-degree (27.8 km at the Equator) spatial resolution to match with the resolution of the climate data. This resulted in a total of 15,459 pixels of which 60% (9,240) are classified as mixed forest, 19% (2,958) as broadleaf deciduous forest, 19% (3,004) as evergreen needleleaf forest, and 2% (257) as deciduous needleleaf forest.

398 **Analysis.** As for the ground-sourced phenology data, climate and soil moisture information at a spatial
399 resolution of 0.25 arc degrees were derived from the Global Land Data Assimilation System (GLDAS)⁴¹.
400 Information on gross primary production (GPP) was extracted from the MODIS Gross Primary Productivity
401 product (MOD17A2H V6)³³, which provides an 8-day composite dataset at 500 m spatial resolution. In total,
402 we included eight variables in our analyses: GPP, LPJ model-derived $A_{net_{day}}$, T_{day} and T_{night} , short-wave
403 radiation, CO₂ levels, precipitation, and soil moisture (at 0–40 cm depth).

404
405 *Seasonal and monthly photosynthesis/climate:* To obtain monthly photosynthesis, T_{day} , and short-wave
406 radiation values, we took the sums (GPP, LPJ model $A_{net_{day}}$, and P model $A_{net_{day}}$) or means (T_{day} , short-
407 wave radiation) of daily values for each month. Similarly, we aggregated values of these variables for six
408 30-day intervals with 10-day moving steps around the June solstice (see 1.5.1 for details).

409
410 Autumn temperature intervals: The optimal autumn intervals at which temperature has the strongest effect
411 on senescence dates were calculated as described in the above section *Analysis of ground-sourced*
412 *European phenology observations – Autumn temperature intervals*. For EOS₅₀ dates, these analyses
413 showed slightly higher R²s and standardized coefficients for T_{day} than for T_{night} (Extended Data Fig. 6b), and,
414 for each time series, we therefore included the respective T_{day} interval with the highest R² in the analyses
415 (hereafter referred to as Autumn T_{day} , Extended Data Fig. 2h,j and Figs. S2h and S4h). For EOS₁₀ dates,
416 we found no delaying effect of any autumn temperature interval (Extended Data Fig. 6a) and we therefore
417 did not control for autumn temperature in the analyses.

418
419 *Models:* To test for the effects of photosynthesis and climate parameters during different times of the year
420 on autumn senescence dates, we ran pixel-level linear models. Both predictor and dependent variables
421 were standardized to obtain relative effect sizes. To run the monthly models, we included the relative
422 photosynthesis/climate value of each month (January to October) in a multivariate model. For the monthly
423 effects of photosynthesis and short-wave radiation on EOS₁₀ dates, only April to September values were
424 included as predictors in the model, with April values representing the sums of January to April (Fig. 2g). To
425 characterize the effects of photosynthesis, T_{day} , and short-wave radiation within 30-day-long intervals
426 around the June solstice on EOS₁₀ dates, we included the variable value within the respective interval as
427 single fixed effect (see e.g., Fig. 2h), whereas we additionally included Autumn T_{day} (to control for autumn
428 temperature) as fixed effect when testing for the effects on EOS₅₀ dates (see e.g., Extended Data Fig. 2).
429 We then ran models including information on pre-solstice (sum of photosynthesis from leaf-out to June 21
430 or mean of T_{day} and radiation from March 20 to June 21) and post-solstice vegetation activity / climate (sum
431 or mean from June 22 to mean senescence date). Models were run separately for photosynthesis, T_{day} and
432 short-wave radiation, and we accounted for possible effects of water availability, atmospheric CO₂
433 concentration, and autumn temperature by additionally including the sums of pre-solstice (March 20 to June
434 21) and post-solstice (June 22 to mean time series senescence date) precipitation, annual CO₂
435 concentration, and Autumn T_{day} (only for EOS₅₀ dates) as fixed effects (full model; Fig. 2f). To test for the
436 explanatory power of pre-solstice variables on inter-annual variation in the timing of EOS, we ran univariate
437 models that included either pre-solstice GPP, T_{day} , radiation, soil moisture or leaf-out date as single effect
438 (Extended Dta Fig. 8).

439 To approximate the end of the period during which early-season vegetation activity exhibited an
440 advancing effect on the onset of senescence, we ran pixel-level linear regression models between gross
441 primary productivity (GPP) and EOS₁₀ dates. GPP summation always started at the day of leaf-out and
442 ended at different dates, using 30-day steps. For each pixel, we then kept the period with the most negative
443 (advancing) effect on EOS₁₀ dates. Extended Data Fig. 4 shows the estimated end date (red line) and
444 starting date (leaf-out date; green line) of this period along latitude, whereby pixel-level estimates were
445 averaged for each degree latitude.

446 To test for decadal-scale temporal trends in EOS dates, we additionally ran mixed effects models
447 where pixels are treated as grouping variables of random intercepts, including only year or year and pre-
448 solstice photosynthesis, temperature or radiation as fixed effects (Fig. 2i–k).

452 **Experiments**

453
454 **Experiment 1 – Seasonal temperature and light manipulation.** The experiment was conducted in Zurich,
455 Switzerland, between March and December 2021. Three-year old *Fagus sylvatica* trees were used to
456 observe the seasonal effects of cooling and shading (9 treatments: 1 control, 4 temperature and 4 shade
457 treatments) on autumn phenology. Plants were obtained from a local nursery in February 2021, transferred
458 to 20 l plastic pots containing a 1:1:1 sand / peat / organic soil mixture with a Nitrogen (N) concentration of
459 ~65 g m⁻³, a Phosphate (P₂O₅) concentration of ~140 g m⁻³, and a Potassium (K₂O) concentration of ~400
460 g m⁻³.

461 We exposed trees to cooling or shading conditions during four 1 month-long periods (30 April – 30
462 May [hereafter referred to as May treatment], 26 May – 25 June [June treatment], 26 June – 26 July [July
463 treatment], and 27 July – 26 August [August treatment]). The experimental and observational unit was a pot
464 with a single individual. The control consisted of 38 trees growing outside under full sun conditions. The
465 treatments consisted of 14 trees each. In the cooling treatments, trees were kept in a climate chamber with
466 a night-time temperature of 5°C and a day-time temperature of 10°C, and simulating ambient day length
467 and light intensities. In the shading treatments, trees were exposed to shade conditions using a shading net
468 that intercepted c. 84% (\pm 10%; mean \pm SD) of the PAR experienced by the control treatment. All trees were
469 watered regularly to keep soil moisture constant.

470 To quantify seasonal changes in leaf chlorophyll content, we measured the relative chlorophyll
471 content at, on average, 4 wk intervals during summer and 1 wk intervals from mid-September until
472 December with a SPAD-502 Plus (Soil Plant Analysis Development, Minolta Camera Co., Ltd, Tokyo,
473 Japan). Per individual, SPAD readings from nine leaves were averaged, whereby we randomly selected
474 three leaves from the top, middle and lower parts of the tree crown. SPAD readings were then transferred
475 to total chlorophyll content (*Chl* in $\mu\text{g/g}$ fresh weight) using an empirically established equation for *Fagus*
476 *sylvatica* leaves⁵⁷:

$$Chl = -0.0029 \times SPAD^2 + 1.175 \times SPAD + 3.8506$$

477 To calculate individual-level leaf chlorophyll content, we additionally included the percentage of leaf
478 abscission in autumn for each individual, that is, the already-dropped leaves in autumn have a chlorophyll
479 content of 0. For example, an individual that lost already 50% of leaves with a chlorophyll content of 30 for
480 the remaining leaves has a total chlorophyll content of 15 (30 \times 0.5). The chlorophyll content between two
481 consecutive measurement dates was estimated using linear interpolation. Finally, we calculated individual
482 leaf senescence dates as the day-of-year when chlorophyll content last fell below 90% (EOS₁₀) or 50%
483 (EOS₅₀) of the maximum chlorophyll content in summer. Because the shading treatment caused short-term
484 changes in chlorophyll content that do not reflect autumn phenological responses, chlorophyll
485 measurements during the treatment until two weeks after the respective treatment period were excluded for
486 the determination of autumn phenology.

487 Leaf net photosynthesis (CO₂ uptake per leaf area) was monitored on a monthly basis from May to
488 July on one leaf of 3–13 individuals per treatment using a portable infrared gas analyzer (LI-6800, Li-
489 Cor, Lincoln, NE) with a 3 x 3 cm leaf chamber. Leaf chamber temperature during the measurements reflected
490 the mean day-time (8.00 – 15.00) temperature experienced by each treatment in the respective month, leaf
491 chamber light intensities reflected the mean light intensities experienced by each treatment in the respective
492 month. Humidity was set to 65%, leaf chamber CO₂ to 400 ppm. Measurements were taken between 2 to
493 6 hours after sunrise with replicate individuals of each treatment done on four consecutive days.

494 To test for differences in leaf senescence dates among treatments, we ran multivariate linear
495 models including temperature and shade treatments as categorical variables.

496 **Experiment 2 – Nutrient and soil moisture manipulation.** The experiment was conducted in Zurich,
497 Switzerland (450 m a.s.l.) between June and December 2020. Sixty three-year old *Fagus sylvatica* trees
498 were obtained from a local nursery in February 2020, transferred to 20 l plastic pots containing a 50/50
499 sand/peat mixture, and kept outdoors under uniform conditions until the start of the experiment (15 June
500 2020). Due to Covid19 restrictions, the experiment could not begin until June 15, but all trees were watered
501 once a week to keep soil moisture constant. During the experiment (June 15 – December 1), all trees were
502 kept outdoors and arranged in randomized blocks.

The experiment followed a 2 x 4 full-factorial design with two nutrient treatments (high versus low nitrogen, phosphorous, and potassium) and four irrigation treatments (High, Intermediate, Low, and No irrigation), resulting in a total of eight treatment combinations (Extended Data Fig. 10). The experimental and observational unit was a pot with a single individual. Each irrigation treatment consisted of 14 individuals of which eight individuals were exposed to high-nutrient and seven to low-nutrient conditions. In the *High Irrigation* treatment, plants were watered regularly (on average, every 3rd day); in the *Intermediate Irrigation* treatment, plants were watered every other time (i.e., every ~6 days); in the *Low Irrigation* treatment, plants were watered every fourth time (i.e., every ~12 days); in the *No Irrigation* treatment, plants were not watered and received only natural precipitation. On June 15 and August 12, the trees of the high-nutrient treatment were fertilized with 20 g organic NPK fertilizer (DCM ECO-XTRA 1), containing 8% nitrogen (1.6 g N), 5% phosphorous (1 g P₂O₅) and 6% potassium (1.2 g K₂O). On July 15, all trees received 0.4 g micronutrients (DCM MICRO-MIX). For each irrigation treatment, soil moisture was measured weekly in 6 randomly chosen individuals. We observed strong differences in soil moisture among the irrigation treatments, with a median soil moisture between June and September of 22.1%, 11.4%, 7.6%. and 4.6% for the *High*, *Intermediate*, *Low*, and *No* irrigation treatments, respectively (Fig. S15a,b).

Leaf chlorophyll content measurements and autumn phenology scoring were done as in Experiment 1. Chlorophyll measurements were conducted at, on average, 2 wk intervals during summer and 1 wk intervals during October.

To test for differences in leaf senescence dates among treatments, we ran multivariate linear models including nutrient and irrigation treatment as categorical variables. We additionally included an interaction term between treatments to test if nutrient or irrigation effects depended on the other treatment but found no significant effect ($P = 0.74$).

References

1. Menzel, A. & Fabian, P. Growing season extended in Europe. *Nature* **397**, 659 (1999).
2. Zohner, C. M., Mo, L., Pugh, T. A. M., Bastin, J. F. & Crowther, T. W. Interactive climate factors restrict future increases in spring productivity of temperate and boreal trees. *Glob. Chang. Biol.* **26**, 4042–4055 (2020).
3. Chuine, I. Why does phenology drive species distribution? *Philos. Trans. R. Soc. B Biol. Sci.* **365**, 3149–3160 (2010).
4. Renner, S. S. & Zohner, C. M. Climate Change and Phenological Mismatch in Trophic Interactions Among Plants, Insects, and Vertebrates. *Annu. Rev. Ecol. Evol. Syst.* **49**, 165–182 (2018).
5. Richardson, A. D. *et al.* Climate change, phenology, and phenological control of vegetation feedbacks to the climate system. *Agric. For. Meteorol.* **169**, 156–173 (2013).
6. Keenan, T. F. *et al.* Net carbon uptake has increased through warming-induced changes in temperate forest phenology. *Nat. Clim. Chang.* **4**, 598–604 (2014).
7. Gallinat, A. S., Primack, R. B. & Wagner, D. L. Autumn, the neglected season in climate change research. *Trends Ecol. Evol.* **30**, 169–176 (2015).
8. Keenan, T. F. & Richardson, A. D. The timing of autumn senescence is affected by the timing of spring phenology: Implications for predictive models. *Glob. Chang. Biol.* **21**, 2634–2641 (2015).
9. Zani, D., Crowther, T. W., Mo, L., Renner, S. S. & Zohner, C. M. Increased growing-season productivity drives earlier autumn leaf senescence in temperate trees. *Science (80-.).* **370**, 1066–1071 (2020).
10. Fu, Y. S. H. *et al.* Variation in leaf flushing date influences autumnal senescence and next year's flushing date in two temperate tree species. *Proc. Natl. Acad. Sci. U. S. A.* **111**, 7355–7360 (2014).
11. Chuine, I. Why does phenology drive species distribution? *Philos. Trans. R. Soc. B Biol. Sci.* **365**, 3149–3160 (2010).
12. Vitasse, Y. *et al.* The great acceleration of plant phenological shifts. *Nat. Clim. Chang.* (2022).
13. Delpierre, N. *et al.* Modelling interannual and spatial variability of leaf senescence for three deciduous tree species in France. *Agric. For. Meteorol.* **149**, 938–948 (2009).
14. Chen, L. *et al.* Leaf senescence exhibits stronger climatic responses during warm than during cold autumns. *Nat. Clim. Chang.* (2020) doi:10.1038/s41558-020-0820-2.

- 559 15. Liu, G., Chen, X., Zhang, Q., Lang, W. & Delpierre, N. Antagonistic effects of growing season and
560 autumn temperatures on the timing of leaf coloration in winter deciduous trees. *Glob. Chang. Biol.*
561 **24**, 3537–3545 (2018).
- 562 16. Zohner, C. M., Rockinger, A. & Renner, S. S. Increased autumn productivity permits temperate
563 trees to compensate for spring frost damage. *New Phytol.* **221**, 789–795 (2019).
- 564 17. Fu, Y. H. *et al.* Larger temperature response of autumn leaf senescence than spring leaf-out
565 phenology. *Glob. Chang. Biol.* **24**, 2159–2168 (2018).
- 566 18. Zohner, C. M. & Renner, S. S. Ongoing seasonally uneven climate warming leads to earlier
567 autumn growth cessation in deciduous trees. *Oecologia* **189**, 549–561 (2019).
- 568 19. Paul, M. J. & Foyer, C. H. Sink regulation of photosynthesis. *J. Exp. Bot.* **52**, 1383–1400 (2001).
- 569 20. Buermann, W. *et al.* Widespread seasonal compensation effects of spring warming on northern
570 plant productivity. *Nature* **562**, 110–114 (2018).
- 571 21. Bigler, C. & Vitasse, Y. Premature leaf discoloration of European deciduous trees is caused by
572 drought and heat in late spring and cold spells in early fall. *Agric. For. Meteorol.* **307**, 108492
573 (2021).
- 574 22. Pyung, O. L., Hyo, J. K. & Hong, G. N. Leaf senescence. *Annual Review of Plant Biology* vol. 58
575 115–136 (2007).
- 576 23. Heide, O. M. Temperature rather than photoperiod controls growth cessation and dormancy in
577 *Sorbus* species. *J. Exp. Bot.* **62**, 5397–5404 (2011).
- 578 24. Fracheboud, Y. *et al.* The Control of Autumn Senescence in European Aspen. *Plant Physiol.* **149**,
579 1982–1991 (2009).
- 580 25. Rossi, S. *et al.* Conifers in cold environments synchronize maximum growth rate of tree-ring
581 formation with day length. *New Phytol.* **170**, 301–310 (2006).
- 582 26. Bauerle, W. L. *et al.* Photoperiodic regulation of the seasonal pattern of photosynthetic capacity
583 and the implications for carbon cycling. *Proc. Natl. Acad. Sci.* **109**, 8612–8617 (2012).
- 584 27. Etzold, S. *et al.* Number of growth days and not length of the growth period determines radial stem
585 growth of temperate trees. *Ecol. Lett.* **00**, 1–13 (2021).
- 586 28. Luo, T. *et al.* Summer solstice marks a seasonal shift in temperature sensitivity of stem growth and
587 nitrogen-use efficiency in cold-limited forests. *Agric. For. Meteorol.* **248**, 469–478 (2018).
- 588 29. Körner, C. *et al.* Where, why and how? Explaining the low-temperature range limits of temperate
589 tree species. *J. Ecol.* **104**, 1076–1088 (2016).
- 590 30. Goulden, M. L., Munger, J. W., Fan, S. M., Daube, B. C. & Wofsy, S. C. Exchange of carbon
591 dioxide by a deciduous forest: Response to interannual climate variability. *Science (80-)*. **271**,
592 1576–1578 (1996).
- 593 31. Zohner, C. M., Renner, S. S., Sebald, V. & Crowther, T. W. How changes in spring and autumn
594 phenology translate into experimental evidence of asymmetric effects. *J. Ecol.* 2717–2728 (2021)
595 doi:10.1111/1365-2745.13682.
- 596 32. Templ, B. *et al.* Pan European Phenological database (PEP725): a single point of access for
597 European data. *Int. J. Biometeorol.* **62**, 1109–1113 (2018).
- 598 33. Running, S., Mu, Q. & Zhao, M. MOD17A2H MODIS/Terra Gross Primary Productivity 8-Day L4
599 Global 500m SIN Grid V006 [Data set]. NASA EOSDIS Land Processes DAAC
600 <https://doi.org/10.5067/MODIS/MOD17A2H.006> (2015).
- 601 34. Stocker, B. D. *et al.* P-model v1.0: An optimality-based light use efficiency model for simulating
602 ecosystem gross primary production. *Geosci. Model Dev.* **13**, 1545–1581 (2020).
- 603 35. Wu, Z. *et al.* Atmospheric brightening counteracts warming-induced delays in autumn phenology of
604 temperate trees in Europe. *Glob. Ecol. Biogeogr.* **30**, 2477–2487 (2021).
- 605 36. Vitasse, Y. *et al.* Impact of microclimatic conditions and resource availability on spring and autumn
606 phenology of temperate tree seedlings. *New Phytol.* **232**, 537–550 (2021).
- 607 37. Massonnet, C. *et al.* Leafy season length is reduced by a prolonged soil water deficit but not by
608 repeated defoliation in beech trees (*Fagus sylvatica* L.): comparison of response among regional
609 populations grown in a common garden. *Agric. For. Meteorol.* **297**, (2021).
- 610 38. Liu, Q. *et al.* Delayed autumn phenology in the Northern Hemisphere is related to change in both
611 climate and spring phenology. *Glob. Chang. Biol.* **22**, 3702–3711 (2016).
- 612 39. Liu, G., Chen, X., Fu, Y. & Delpierre, N. Modelling leaf coloration dates over temperate China by

- 613 considering effects of leafy season climate. *Ecol. Model.* **394**, 34–43 (2019).
- 614 40. Vitasse, Y., Signarbieux, C. & Fu, Y. H. Global warming leads to more uniform spring phenology
615 across elevations. *Proc. Natl. Acad. Sci.* 201717342 (2017) doi:10.1073/pnas.1717342115.
- 616 41. Rodell, M. *et al.* The Global Land Data Assimilation System. *Bull. Am. Meteorol. Soc.* **85**, 381–394
617 (2004).
- 618 42. Luedeling, E. chillR: Statistical Methods for Phenology Analysis in Temperate Fruit Trees. (2021).
- 619 43. Meinshausen, M. *et al.* Historical greenhouse gas concentrations for climate modelling (CMIP6).
620 *Geosci. Model Dev.* **10**, 2057–2116 (2017).
- 621 44. Hengl, T. *et al.* SoilGrids250m: Global gridded soil information based on machine learning. *PLoS
622 One* **12**, e0169748 (2017).
- 623 45. Sitch, S. *et al.* Evaluation of ecosystem dynamics, plant geography and terrestrial carbon cycling in
624 the LPJ dynamic global vegetation model. *Glob. Chang. Biol.* **9**, 161–185 (2003).
- 625 46. Moeyns, J. soiltexture: Functions for Soil Texture Plot, Classification and Transformation. (2018).
- 626 47. Smith, B. *et al.* Implications of incorporating N cycling and N limitations on primary production in an
627 individual-based dynamic vegetation model. *Biogeosciences* **11**, 2027–2054 (2014).
- 628 48. Huang, M. *et al.* Air temperature optima of vegetation productivity across global biomes. *Nat. Ecol.
629 Evol.* **3**, 772–779 (2019).
- 630 49. Xie, Y., Wang, X., Wilson, A. M. & Silander, J. A. Predicting autumn phenology: How deciduous
631 tree species respond to weather stressors. *Agric. For. Meteorol.* **250–251**, 127–137 (2018).
- 632 50. Gerten, D., Schaphoff, S., Haberlandt, U., Lucht, W. & Sitch, S. Terrestrial vegetation and water
633 balance—hydrological evaluation of a dynamic global vegetation model. *J. Hydrol.* **286**, 249–270
634 (2004).
- 635 51. Prentice, I. C., Dong, N., Gleason, S. M., Maire, V. & Wright, I. J. Balancing the costs of carbon
636 gain and water transport: Testing a new theoretical framework for plant functional ecology. *Ecol.
637 Lett.* **17**, 82–91 (2014).
- 638 52. Wang, H. *et al.* Towards a universal model for carbon dioxide uptake by plants. *Nat. Plants* **3**, 734–
639 741 (2017).
- 640 53. Bates, D., Mächler, M., Bolker, B. & Walker, S. Fitting linear mixed-effects models using lme4. *J.
641 Stat. Softw.* **67**, 1–48 (2015).
- 642 54. Mann, H. B. Nonparametric tests against trend. *Econometrica* **13**, 245–259 (1945).
- 643 55. Friedl, M., Gray, J. & Sulla-Menashe, D. MCD12Q2 MODIS/Terra+Aqua Land Cover Dynamics
644 Yearly L3 Global 500m SIN Grid V006. distributed by NASA EOSDIS Land Processes DAAC
645 <https://doi.org/10.5067/MODIS/MCD12Q2.006> (2019).
- 646 56. Friedl, M. & Sulla-Menashe, D. MCD12Q1 MODIS/Terra+Aqua Land Cover Type Yearly L3 Global
647 500m SIN Grid V006. distributed by NASA EOSDIS Land Processes DAAC
648 <https://doi.org/10.5067/MODIS/MCD12Q1.006> (2019).
- 649 57. Percival, G. C., Keary, I. P. & Noviss, K. The potential of a chlorophyll content SPAD meter to
650 quantify nutrient stress in foliar tissue of sycamore (*Acer pseudoplatanus*), English oak (*Quercus
651 robur*), and European beech (*Fagus sylvatica*). *Arboric. Urban For.* **34**, 89–100 (2008).

655 **Acknowledgements**

656 CMZ was funded by the Ambizione grant PZ00P3_193646. TWC was funded by DOB Ecology. DP was
657 supported by the Faculty of Science Foundation of the Charles University and the Hlávka Foundation. YHF
658 was supported by the National Science Fund for Distinguished Young Scholars (42025101). We thank
659 Christian Körner and V. Sebald for comments on the manuscript.

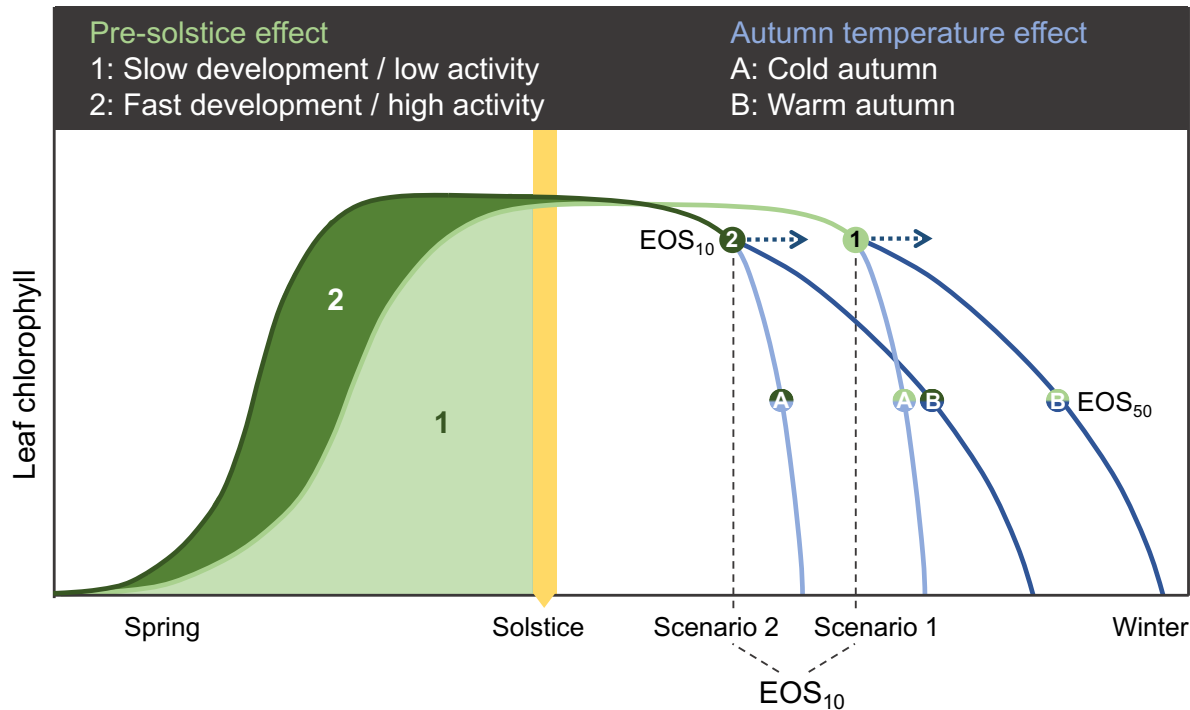
660 **Statement of authorship:** CMZ conceived and developed the study and wrote the first draft of the
661 manuscript. LM contributed to the development of the study and the remote-sensing analysis. RB, DP and
662 CMZ conducted the experiments. LMo contributed to the analysis. TWC, SSR, LM, YV, YHF and BDS
663 contributed to the writing.

664

666 **Data and materials availability:** All source code and experimental data are available on github
667 (<https://github.com/ConstantinZohner/AutumnPhenologySPS>). The PEP725 data used for this study are
668 freely available at www.PEP725.eu. The satellite-derived phenology observations are freely available at
669 <https://doi.org/10.5067/MODIS/MCD12Q2.006>.

670
671 **Competing interests:** The authors declare that there are no competing interests.
672

673 **Figures**
674
675
676



677
678 **Fig. 1. Conceptual model of autumn phenological responses to pre-solstice and post-solstice**
679 **growth and temperature (Solstice-as-Phenology-Switch [SPS] hypothesis).** The onset of autumnal
680 senescence is estimated in this study as the date when the greenness index last dropped by >10% of the
681 seasonal maximum (end-of-season, EOS_{10}). In northern forests, stem growth and development rates and
682 photosynthetic capacity are highest before the summer solstice and decline with shortening days^{25–27}, the
683 adaptive reason being the limited time remaining for tissue maturation and bud set before the first frost.
684 According to the model, inter-annual variation in EOS_{10} should be a function of pre-solstice growth due to
685 developmental constraints on leaf longevity, with later EOS_{10} in years with slow development / low activity
686 before the solstice (scenario 1) and earlier EOS_{10} in years with fast development / high activity (scenario 2).
687 The progression of leaf senescence varies with autumn temperature, with faster chlorophyll breakdown in
688 cold-autumn years (scenario A) than in warm-autumn years (scenario B), and the dates of 50% chlorophyll
689 loss (EOS_{50}) are therefore the combined result of pre- and post-solstice effects. An earlier start of
690 senescence in high-activity years (scenario 2) also predicts that trees will become sensitive to autumn
691 cooling earlier than in low-activity years (see blue arrows). Four fundamental predictions arise from this
692 model that were tested in this study: 1) Enhanced pre-solstice vegetation activity should drive earlier EOS_{10}
693 (scenario 1 *versus* 2). 2) There should be a reversal of growth and temperature effects around the time of
694 the summer solstice. 3) Autumn temperature should affect the speed of senescence and thus have a
695 delaying effect on EOS_{50} dates (scenario A *versus* B), but only little effect on EOS_{10} dates. 4) The date when
696 trees become sensitive to autumn temperature (blue arrows) should have advanced over recent decades
697 because of an earlier onset of senescence (EOS_{10}).

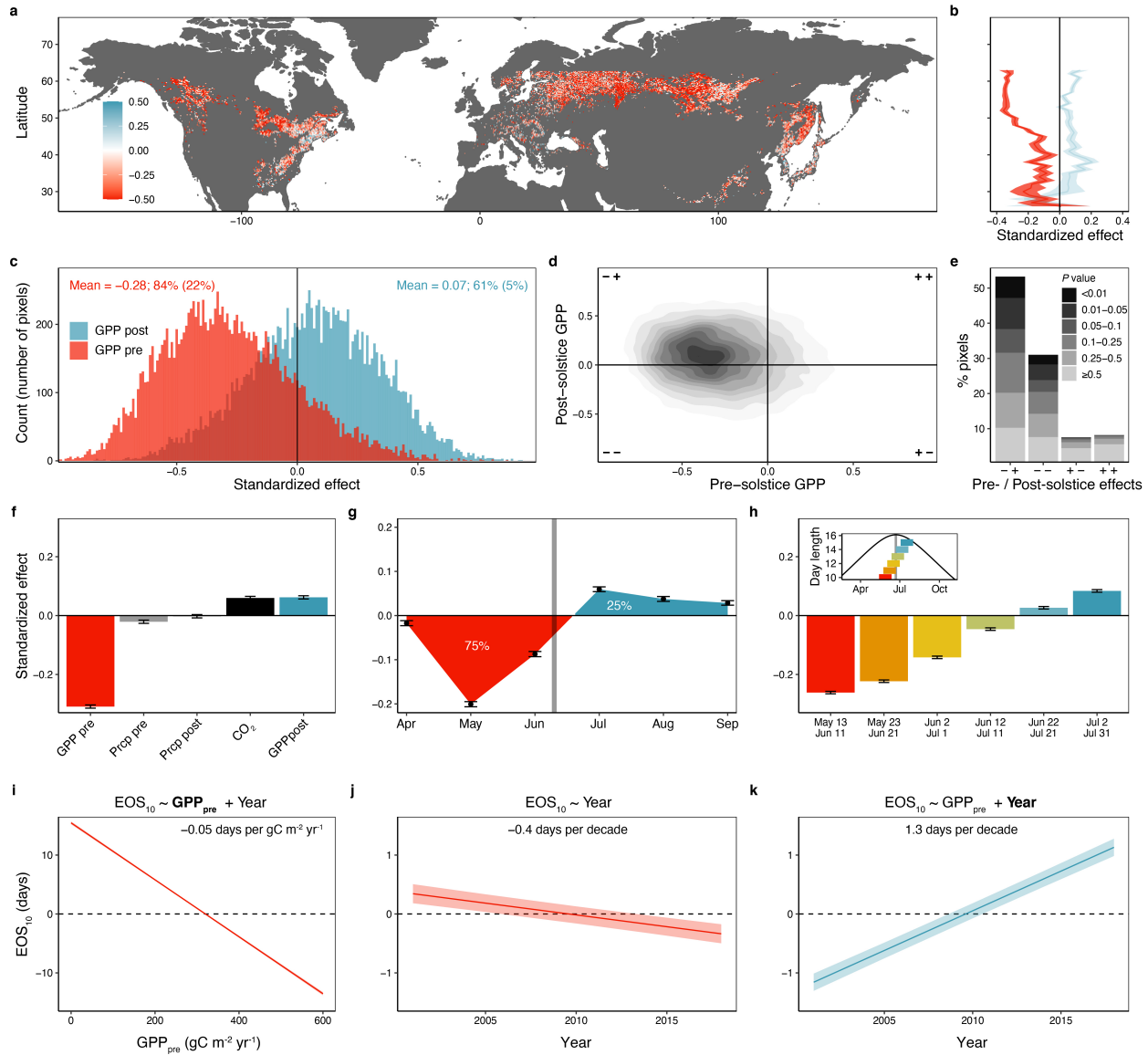


Fig. 2. Satellite observations reveal consistent advances in the onset of senescence (EOS_{10}) across northern forests in response to enhanced pre-solstice vegetation activity. **a**, Map showing the standardized effects of pre-solstice (leaf-out to solstice) gross primary productivity (GPP) on EOS_{10} timing at 0.25° resolution from linear models, including pre-solstice GPP and post-solstice (solstice to mean senescence) GPP as predictor variables. Red pixels indicate an earlier EOS_{10} under enhanced pre-solstice GPP, blue pixels indicate a delayed EOS_{10} . **b**, Effect size means and 95% confidence ranges summarized for each degree latitude (pre-solstice effects in red, post-solstice effects in blue). **c**, The distribution of the pre-solstice and post-solstice GPP effects across all pixels. Mean pre- and post-solstice GPP effect sizes and the percentage of pixels with an advancing pre-solstice GPP effect or delaying post-solstice GPP effect shown as red and blue text, respectively (percentage of significant pixels at $P < 0.05$ in brackets). **d**, Two-dimensional density plot of pre- and post-solstice GPP effects. **e**, Barplot summarizing the effect direction across all analysed pixels. Grey scale indicates significance levels of pre-solstice GPP effects. **f**, The effects of pre-solstice and post-solstice GPP, pre-solstice (21 March to solstice) and post-solstice precipitation (prcp), and atmospheric CO_2 . **g**, Relationship between monthly GPP and EOS_{10} dates. Percentages reflect the total positive and negative areas under the curve, i.e., the relative advancing versus delaying effects of

714 seasonal GPP. **h**, The univariate effects of one-month-long GPP intervals around the summer solstice (May
715 13 to June 11, May 23 to June 21, June 2 to July 1, June 12 to July 11, June 22 to July 21, and July 2 to
716 July 31; see inset). Analyses in **f–h** show effect size means and 95% confidence ranges from pixel-level
717 linear models with both predictor and dependent variables standardized. **i–j**, Mean effects ($\pm 95\%$ confidence
718 ranges) of pre-solstice GPP and year on EOS_{10} anomalies from mixed effects models where pixels are
719 treated as grouping variables of random intercepts. **i**, Partial effect of pre-solstice GPP on EOS_{10} anomalies,
720 including both pre-solstice GPP and year as fixed effects. **j**, Temporal trend in EOS_{10} anomalies with year
721 as single fixed effect. **k**, Partial effect of year on EOS_{10} anomalies, where both pre-solstice GPP and year
722 are treated as fixed effects.
723

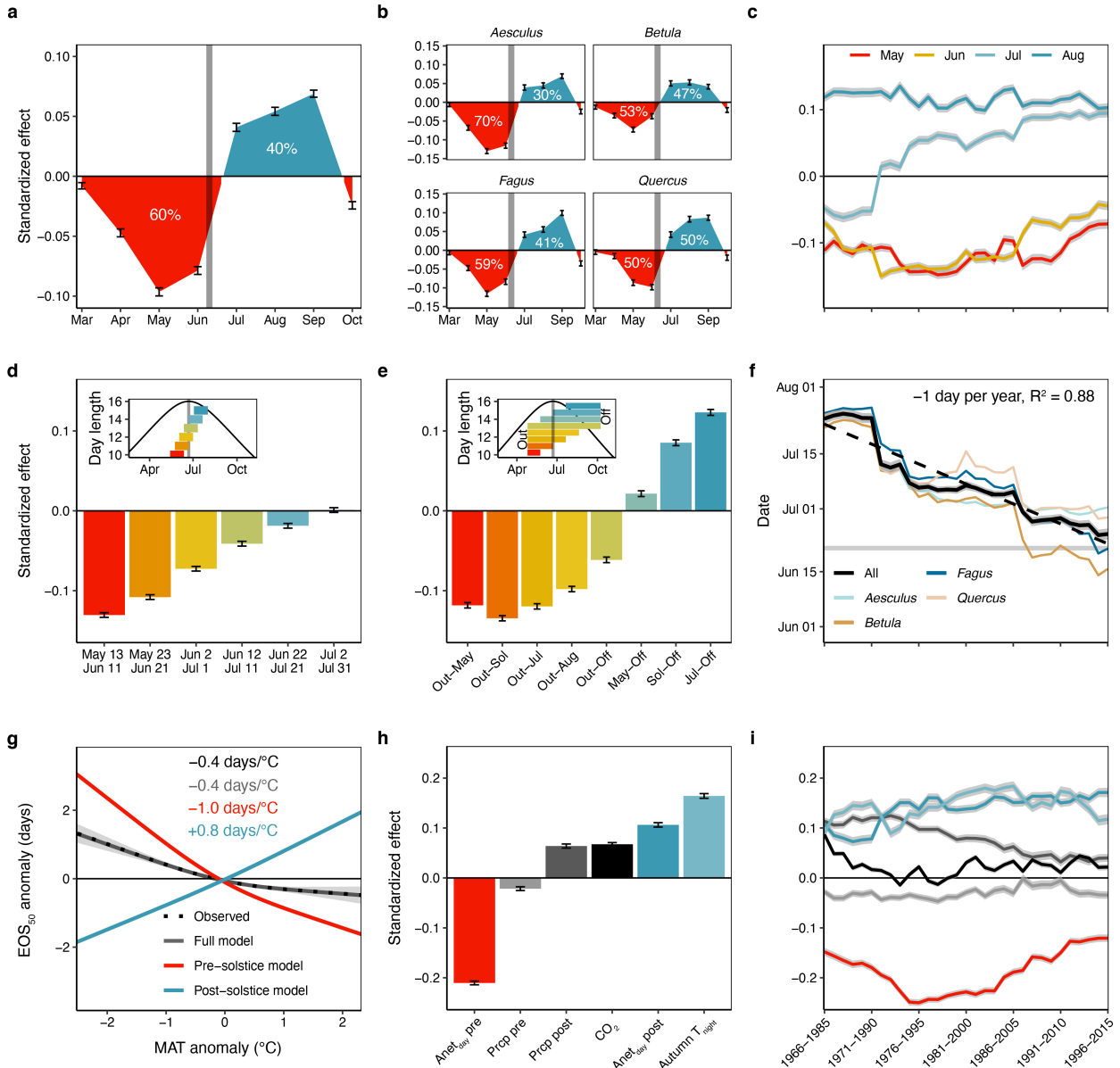
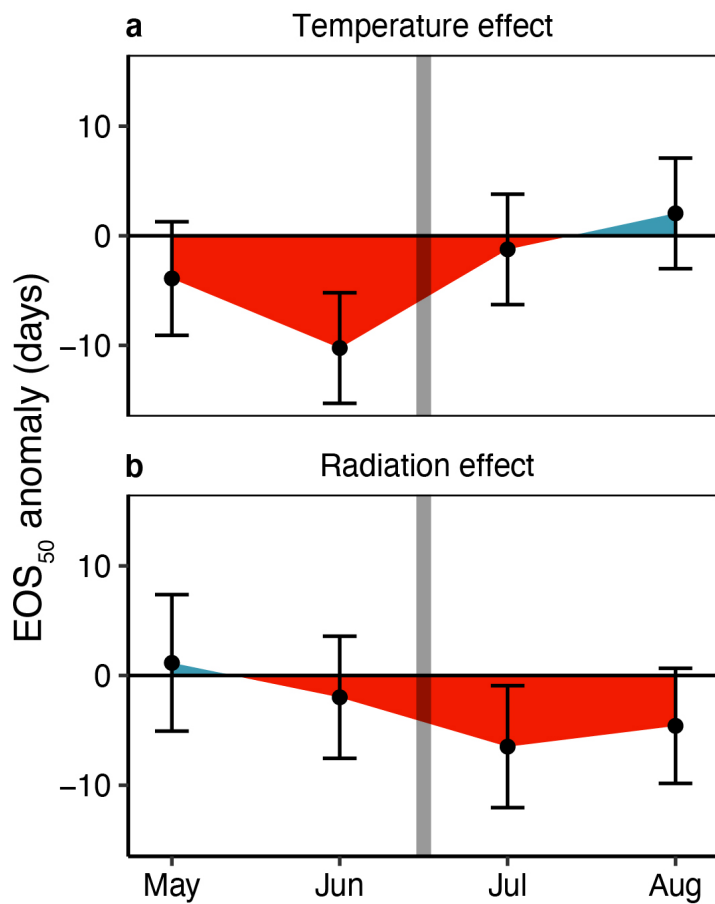
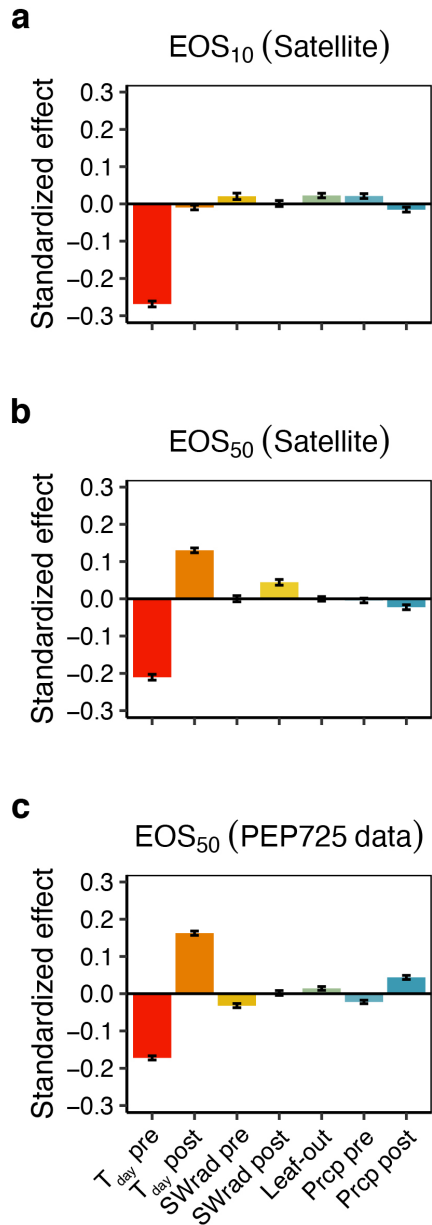


Fig. 3. Relationships between seasonal photosynthesis and the timing of mid-senescence (EOS₅₀) from European long-term observations (PEP725 data). **a**, Effects of monthly (March to October) photosynthesis on EOS₅₀ dates. Percentages reflect the relative advancing versus delaying effects of seasonal photosynthesis on EOS₅₀ dates. **b**, Species-level results with percentages as in panel a. **c**, Moving-window analysis, showing the effects of May (leaf-out to 31 May), June, July, and August/September (1 August to 30 September) photosynthesis for each 20-year time period from 1966 to 2015. **d**, Effects of one-month-long photosynthesis intervals around the summer solstice (May 13 to June 11, May 23 to June 21, June 2 to July 1, June 12 to July 11, June 22 to July 21, and July 2 to July 31; see inset), including the respective photosynthesis interval and autumn night-time temperature (Autumn T_{night}) as fixed effects. **e**, The effects of cumulative photosynthesis from leaf-out to May 22 (Out-May), leaf-out to solstice (Out-Sol), leaf-out to July 21 (Out-Jul), leaf-out to August 20 (Out-Aug), leaf-out to mean EOS₅₀ (Out-Off), May 22 to mean EOS₅₀ (May-Off), solstice to mean EOS₅₀ (Sol-Off), and July 21 to mean EOS₅₀ (Jul-Off), including the respective photosynthesis interval as single fixed effect. **f**, Moving-window analysis, showing the 'reversal' dates when the photosynthesis effect switches from negative to positive for each 20-year time period.

739 period from 1966 to 2015 (based on monthly correlations, see panels **a–c**). On average, the reversal date
740 advanced by 1 day per year. **g–i**, The effects of pre-solstice (leaf-out to solstice) and post-solstice (solstice
741 to mean EOS₅₀) photosynthesis, pre-solstice (21 March to solstice) and post-solstice precipitation,
742 atmospheric CO₂, and Autumn T_{night}. **g**, Model predictions in response to mean annual temperature (MAT)
743 anomalies (black dashed line: observed trend; black solid line: full model prediction including pre- and post-
744 solstice effects; red line: model prediction including only pre-solstice photosynthesis and precipitation and
745 CO₂ as predictors; blue line: model prediction including only post-solstice photosynthesis and precipitation,
746 CO₂, and Autumn T_{night}). **h**, Standardised effects. **i**, 20-year moving-window analysis of the effects (colours
747 as in panel **h**). Analyses show effect size means \pm 2 s.e. from linear mixed models, including time series
748 and species (**a,c–i**) or only time series (**b,f**) as random effects, with both predictor and dependent variables
749 standardized.
750



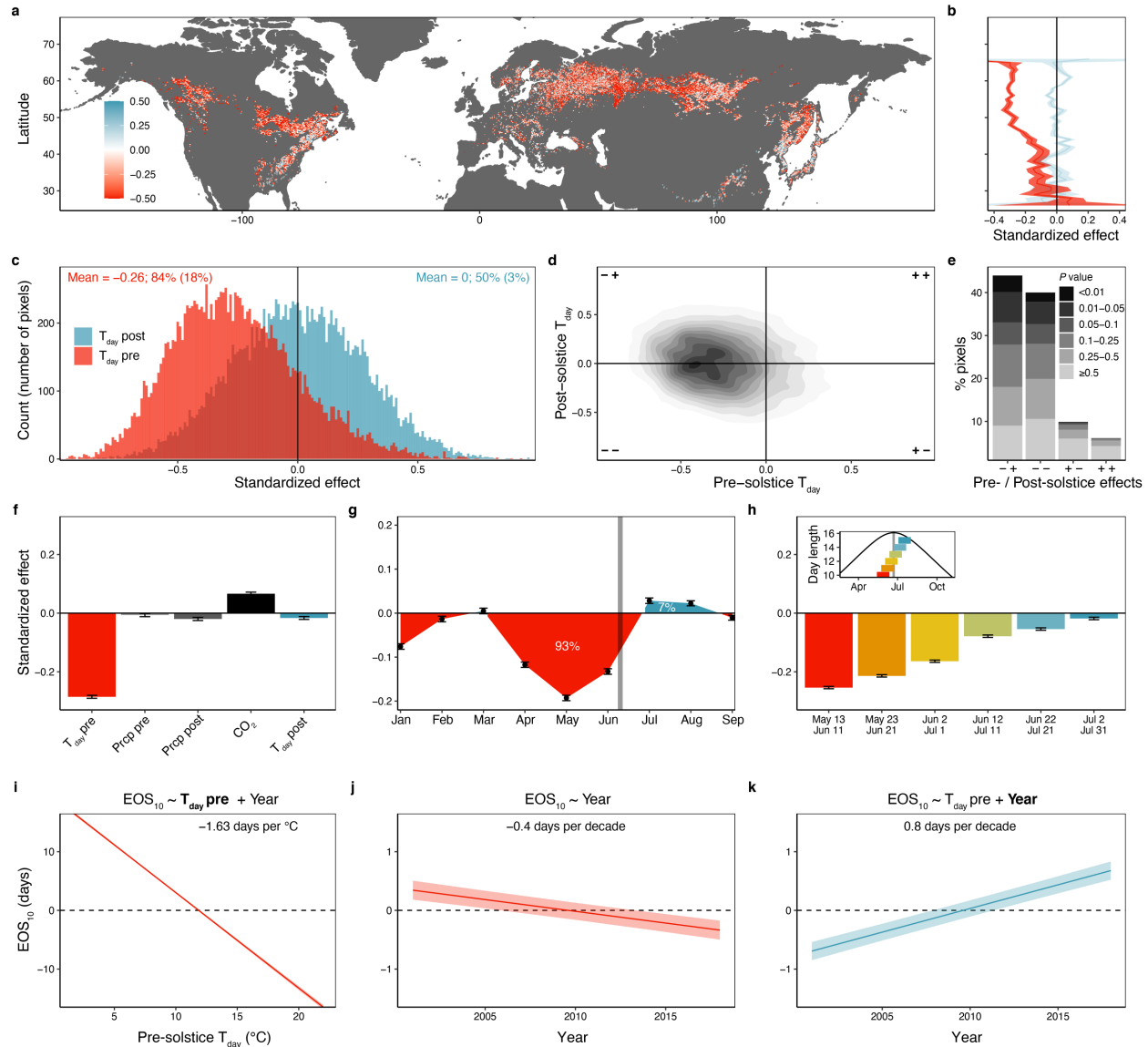
751
 752 **Fig. 4. The seasonal effects of temperature (a) and shading (b) on autumn phenology in European**
 753 **beech from experiment 1.** Effects of monthly (May to August) cooling (a) and shading (b) treatments on
 754 EOS₅₀ dates. Analyses show effect size means \pm 95% confidence intervals from linear models, including
 755 treatment as fixed effect. Note that effect directions were reversed to facilitate comparison with Figs. 2 and
 756 3, i.e., negative values indicate EOS₅₀ advances under warmer (a) or brighter (b) conditions. See methods
 757 for details.
 758



759
760
761
762
763
764
765
766
767

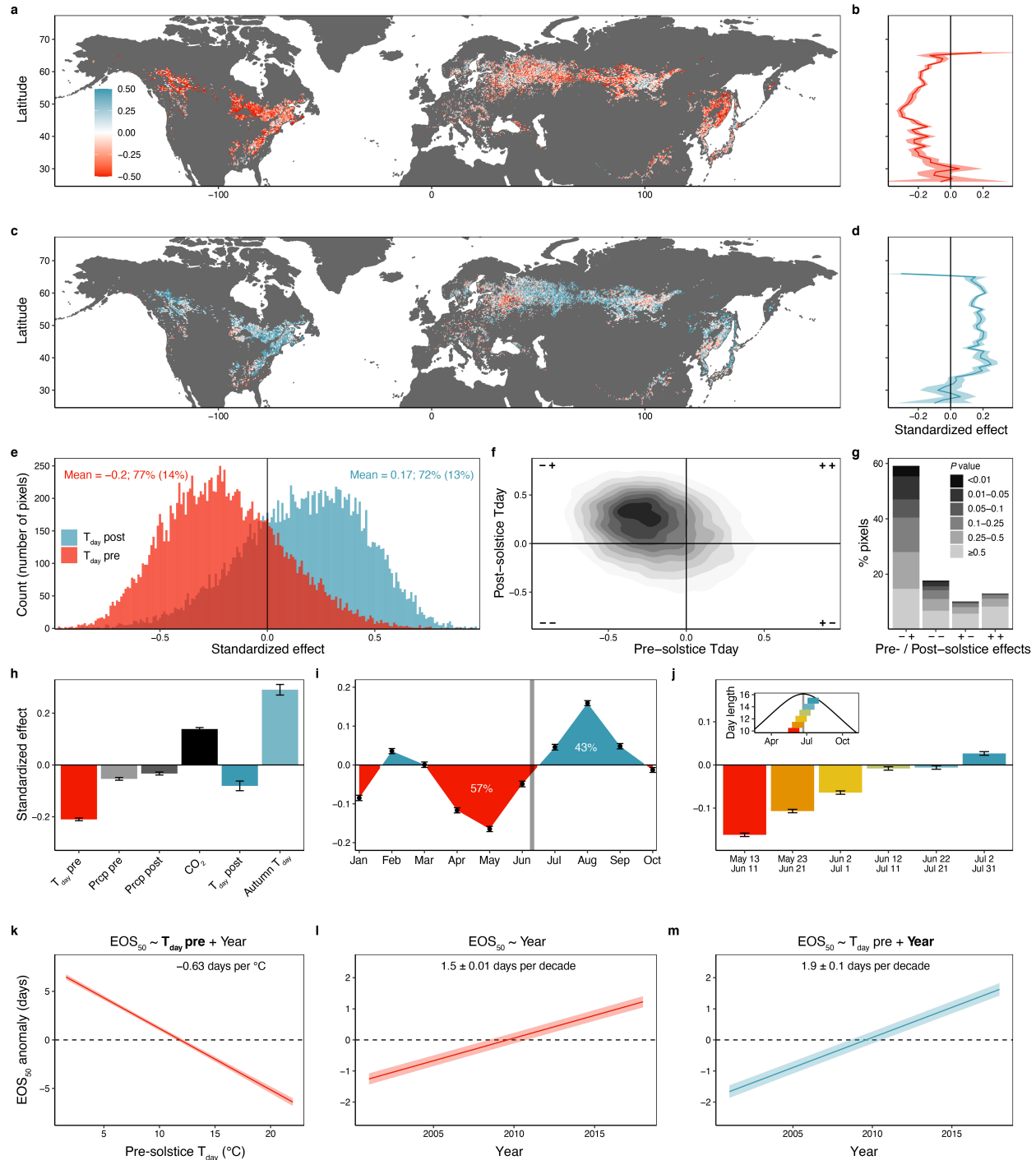
Fig. 5. The effects of pre- and post-solstice temperature, radiation, water availability and spring leaf-out dates on inter-annual variation in the timing of EOS₁₀ (a) and EOS₅₀ (b, c). We ran linear models including mean day-time temperature (T_{day}) and short-wave radiation (SWrad) and the sums of precipitation (prcp) from March 20 to June 21 (pre-solstice) and from June 22 to the mean EOS date of each time series (post-solstice) as well as spring leaf-out dates as predictor variables. Models were run at the pixel-level (a, b) or individual-level (c) and the mean effects (\pm 95% confidence intervals) are shown. All variables were standardized to allow for effect size comparison.

768 **Extended Data Figures**
769



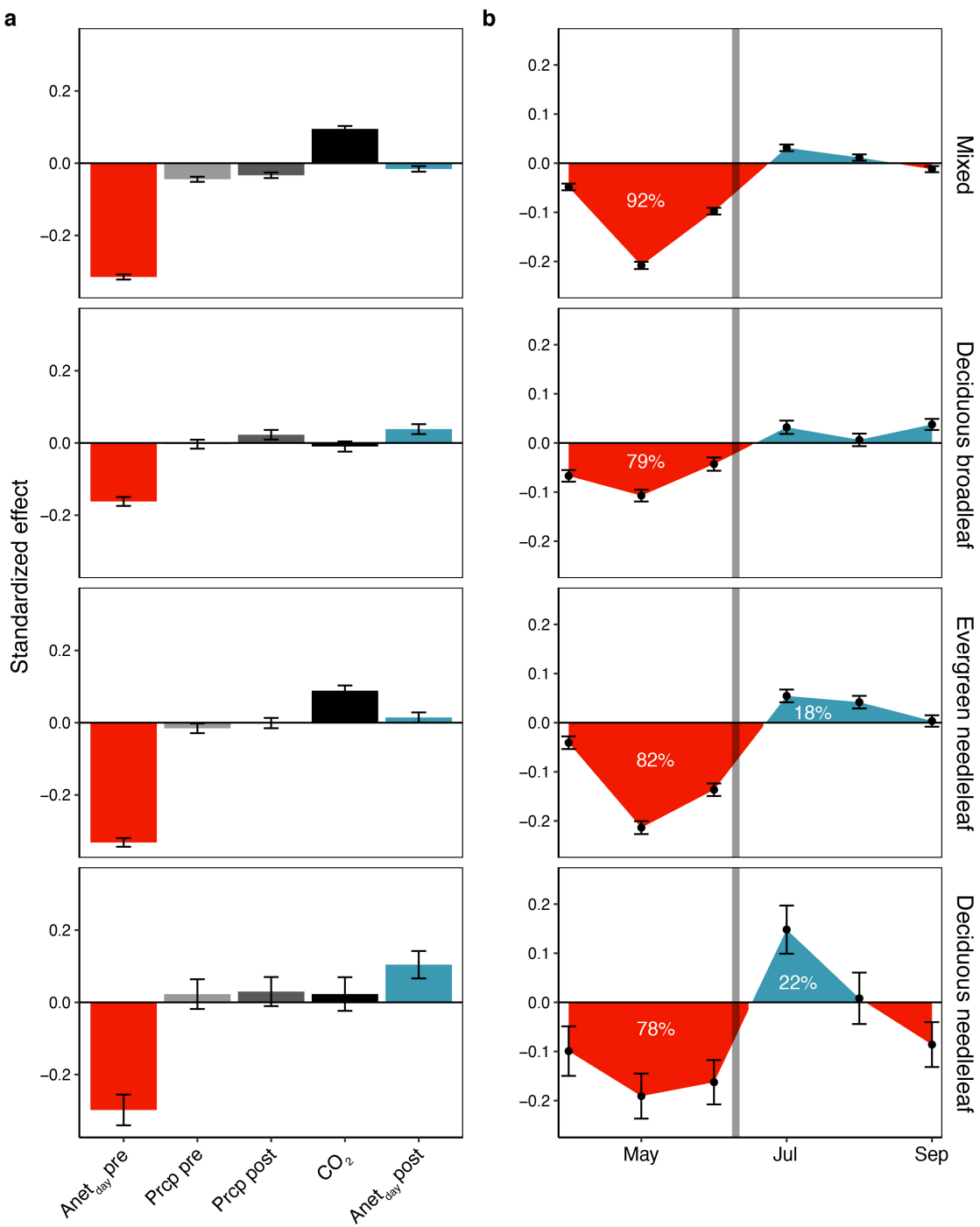
Extended Data Fig. 1. The seasonal effects of day-time temperature (T_{day}) on inter-annual variation in senescence onset (EOS₁₀ dates) [same as Fig. 2 but using T_{day} as predictor variable]. **a**, Map showing the standardized effects of pre-solstice (leaf-out to solstice) T_{day} on EOS₁₀ timing at 0.25° resolution from linear models, including pre-solstice T_{day} and post-solstice (solstice to mean senescence) T_{day} as predictor variables. Red pixels indicate an earlier EOS₁₀ under enhanced pre-solstice T_{day} , blue pixels indicate a delayed EOS₁₀. **b**, Effect size means and 95% confidence ranges summarized for each degree latitude (pre-solstice effects in red, post-solstice effects in blue). **c**, The distribution of the pre-solstice and post-solstice T_{day} effects across all pixels. Mean pre- and post-solstice T_{day} effect sizes and the percentage of pixels with a negative pre-solstice T_{day} or positive post-solstice T_{day} effect (percentage of significant pixels at $P < 0.05$ in brackets) shown as red and blue text, respectively. **d**, Two-dimensional density plot of pre- and post-solstice T_{day} effects. **e**, Barplot summarizing the effect direction across all analysed pixels. Grey scale indicates significance levels of pre-solstice T_{day} effects. **f**, The effects of pre-solstice and post-solstice T_{day} , pre-solstice (21 March to solstice) and post-solstice precipitation, and atmospheric CO₂. **g**, Relationship between monthly T_{day} and EOS₁₀ dates. Percentages reflect the total positive and negative areas under the curve, i.e., the relative advancing versus delaying effects of seasonal T_{day} . **h**, The univariate effects of one-month-long T_{day} intervals around the summer solstice (May 13 to June 11, May 23 to June 21, June 2 to July 1, June 12 to July 11, June 22 to July 21, and July 2 to July 31; see inset). Analyses in **f-h** show effect size means and 95% confidence ranges from pixel-level linear models with both predictor and dependent variables standardized. **i-j**, Mean effects ($\pm 95\%$ confidence ranges) of pre-solstice T_{day} and year on EOS₁₀ anomalies from mixed effects models where pixels are treated as grouping variables of random intercepts. **i**, Partial effect of pre-solstice T_{day} , including both pre-solstice T_{day} and year as fixed effects. **j**, Temporal trend in EOS₁₀ anomalies with year as single fixed effect. **k**, Partial effect of year, where both pre-solstice T_{day} and year are treated as fixed effects.

770
771
772
773
774
775
776
777
778
779
780
781
782
783
784
785
786
787
788
789

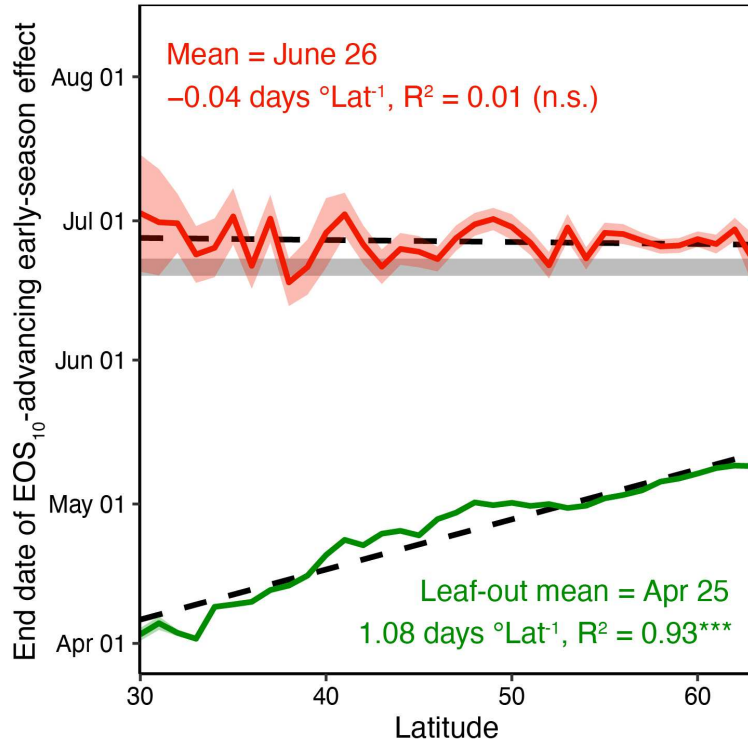


Extended Data Fig. 2. The seasonal effects of T_{day} on inter-annual variation in mid-senescence (EOS_{50} dates). a, c, Maps showing the standardized effects of pre-solstice T_{day} (leaf-out to solstice; a) and post-solstice T_{day} (solstice to mean EOS_{50} , b) on EOS_{50} timing at 0.25° resolution from linear models, including pre-solstice T_{day} and post-solstice T_{day} as predictor variables. Red pixels indicate an earlier EOS_{50} under higher pre-solstice or post-solstice T_{day} , respectively, blue pixels indicate a delayed EOS_{50} . b, d, Effect size means and 95% confidence ranges summarized for each degree latitude (pre-solstice effects in red (b), post-solstice effects in blue (d)). e, The distribution of the pre-solstice and post-solstice T_{day} effects across all pixels. Mean pre- and post-solstice T_{day} effect sizes and the percentage of pixels with a negative pre-solstice T_{day} or positive post-solstice T_{day} effect (percentage of significant pixels at $P < 0.05$ in brackets) shown as red and blue text, respectively. f, Two-dimensional density plot of pre- and post-solstice T_{day} effects. g, Barplot summarizing the effect direction across all analysed pixels. Grey scale indicates significance levels of pre-solstice T_{day} effects. h, The effects of pre-solstice and post-solstice T_{day} , pre-solstice (21 March to solstice) and post-solstice precipitation, atmospheric

801 CO₂, and autumn T_{day}. **i**, Relationship between monthly T_{day} and EOS₅₀ dates. Percentages reflect the total positive and negative areas
802 under the curve, i.e., the relative advancing versus delaying effects of seasonal T_{day}. **j**, The univariate effects of one-month-long T_{day}
803 intervals around the summer solstice (May 13 to June 11, May 23 to June 21, June 2 to July 1, June 12 to July 11, June 22 to July 21,
804 and July 2 to July 31; see inset). Analyses in **h–j** show effect size means and 95% confidence ranges from pixel-level linear models
805 with both predictor and dependent variables standardized. **k–m**, Mean effects ($\pm 95\%$ confidence ranges) of pre-solstice T_{day} and year
806 on EOS₅₀ anomalies from mixed effects models where pixels are treated as grouping variables of random intercepts. **k**, Partial effect
807 of pre-solstice T_{day}, including both pre-solstice T_{day} and year as fixed effects. **l**, Temporal trend in EOS₅₀ anomalies with year as single
808 fixed effect. **m**, Partial effect of year, where both pre-solstice T_{day} and year are treated as fixed effects.
809

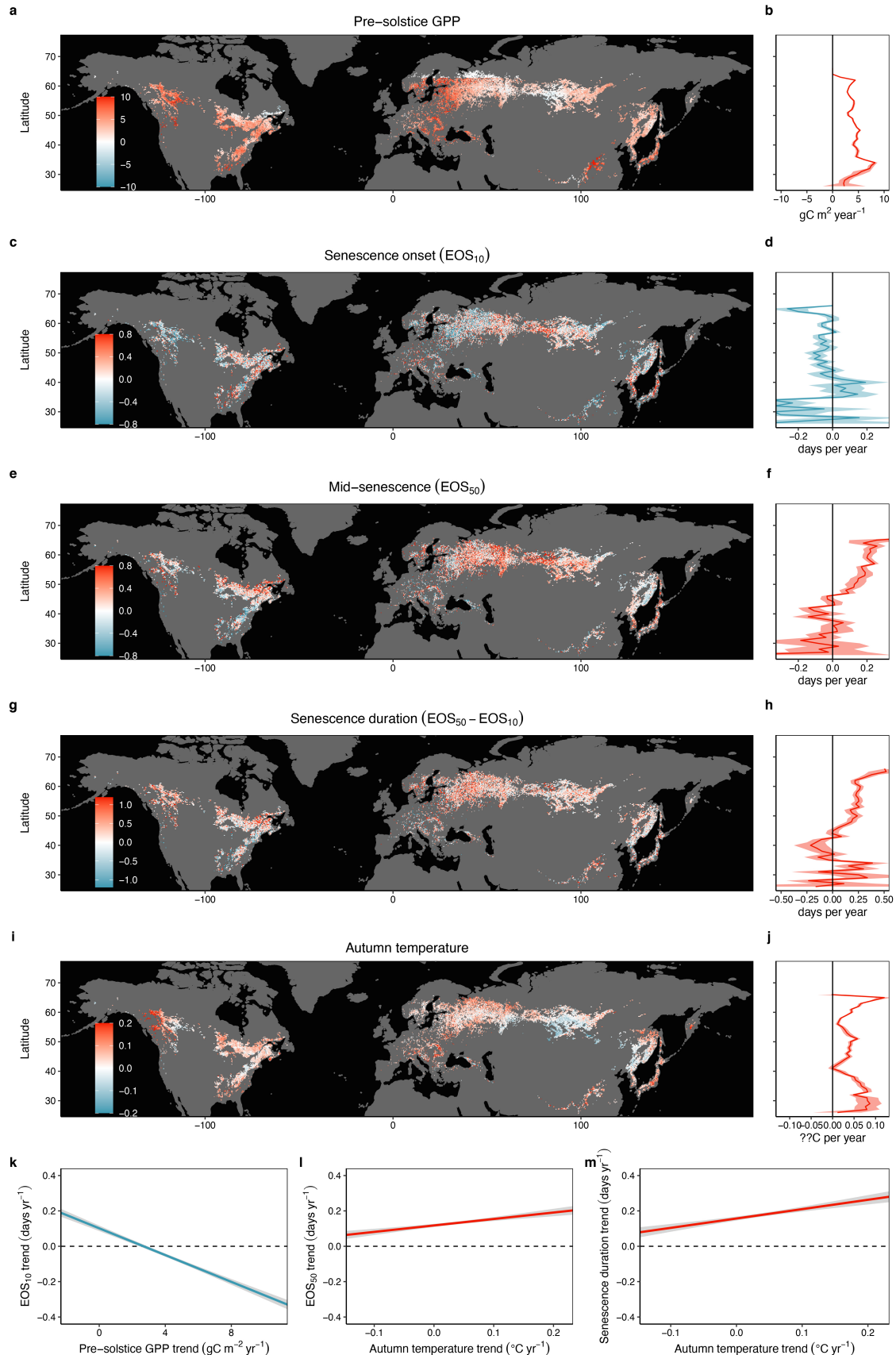


810
 811 **Extended Data Fig. 3. Relationships between seasonal productivity (Anet_{day}) and the timing of**
 812 **senescence onset (EOS₁₀) within mixed, deciduous broadleaf, deciduous needleleaf, and evergreen**
 813 **needleleaf forests.** a, The effects of pre-solstice and post-solstice Anet_{day}, pre-solstice (21 March to
 814 solstice) and post-solstice precipitation, and atmospheric CO₂ on EOS₁₀ dates. b, Relationship between
 815 monthly Anet_{day} and EOS₁₀ dates. Percentages reflect the total positive and negative areas under the curve,
 816 i.e., the relative advancing versus delaying effects of seasonal Anet_{day}.
 817

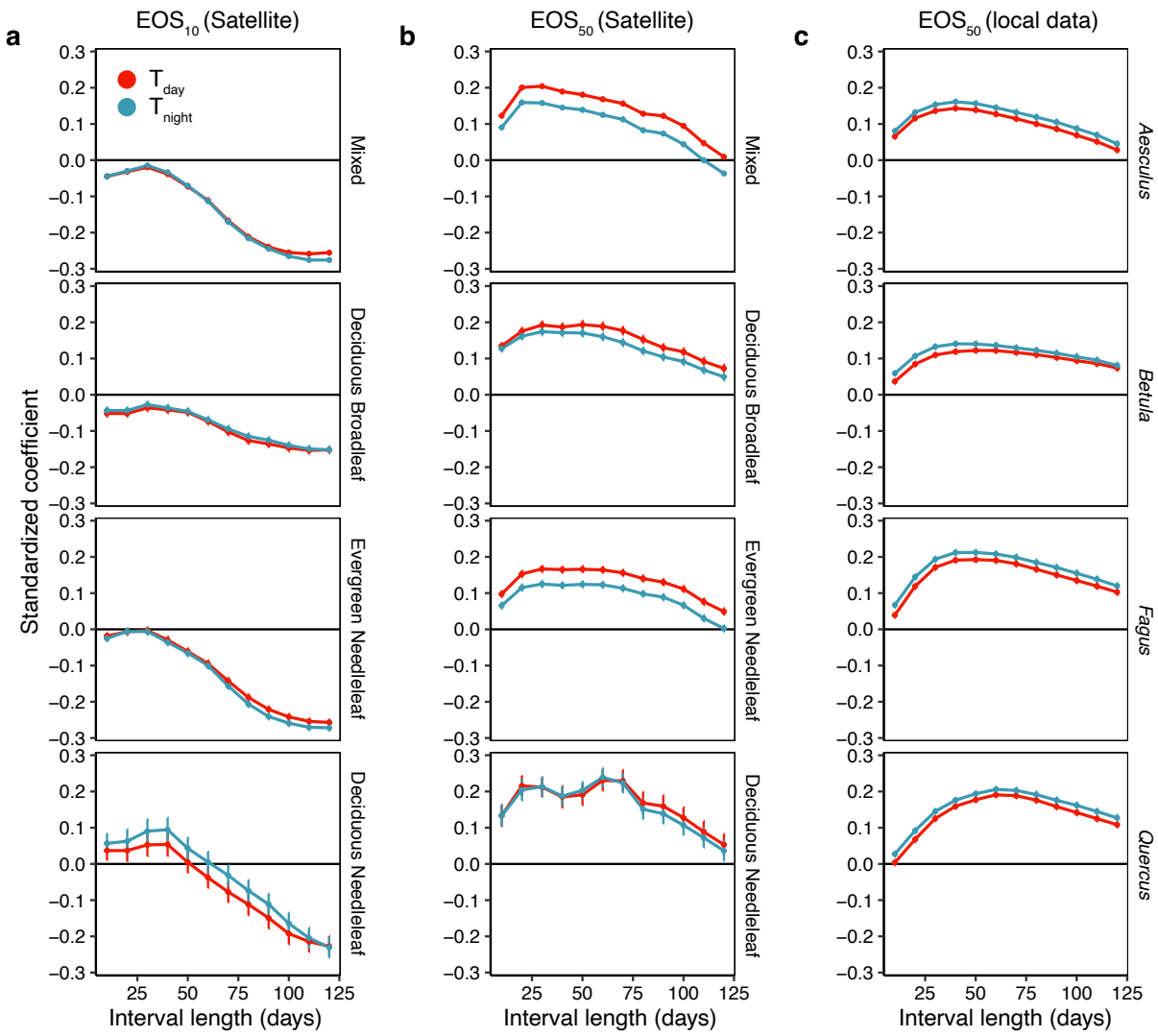


818
819
820 **Extended Data Fig. 4. End date (red line) of the early-season growth period exhibiting an advancing**
821 **effect on the onset of senescence (EOS₁₀).** Pixel-level linear regression models were applied to test for
822 the effect of gross primary productivity (GPP) on EOS₁₀ dates. GPP summation always started at leaf-out
823 and ended at different dates, using 30-day steps. For each pixel, we then obtained the period that showed
824 the most negative effect on EOS₁₀ dates. The red line shows the end date of this period along latitude,
825 whereby pixel-level estimates were averaged for each degree latitude. Across the entire latitudinal range,
826 the end date of the early-season effect consistently occurred right after the summer solstice at June ~26.
827 Red text shows the mean date as well as the slope and R² for the correlation between latitude and the end
828 date of the early-season effect ($R^2 = 0.01$). The green line represents the average spring leaf-out dates for
829 each degree latitude, showing an average delay in leaf-out of 1.08 days per each degree increase in
830 northern latitude ($R^2 = 0.93$). Grey line represents the summer solstice (21 June). Non-significant (n.s.): P
831 > 0.05; *** P < 0.001.

832

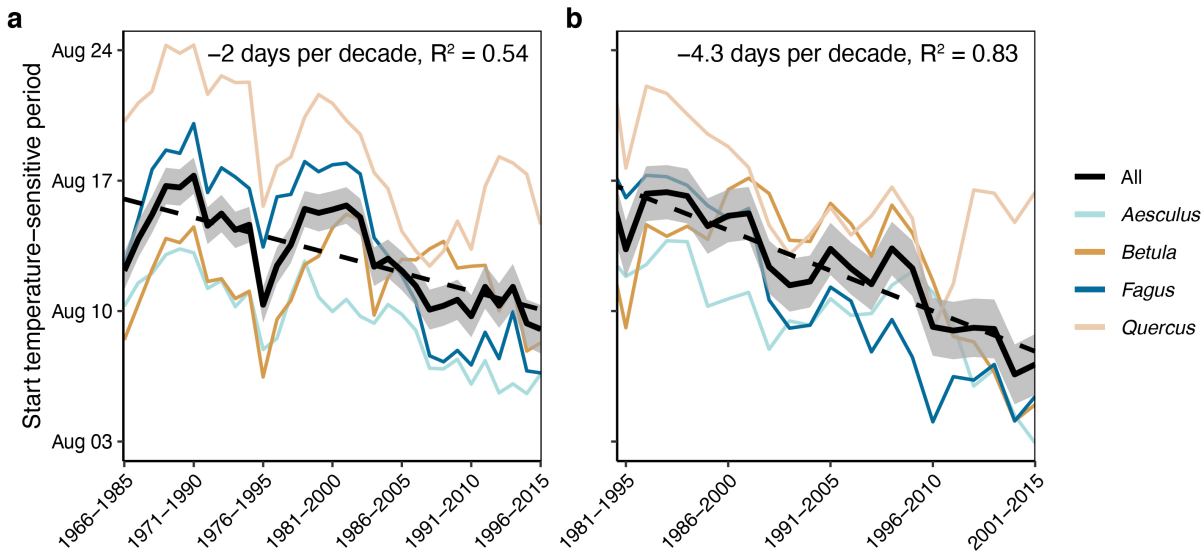


834 **Extended Data Fig. 5. Temporal trends in (a) pre-solstice gross primary productivity [GPP], (c)**
835 **senescence onset (EOS_{10}) dates, (e) mid-senescence (EOS_{50}) dates, (g) senescence duration (EOS_{10} -**
836 **to- EOS_{50}) and (i) autumn temperature at 0.25° resolution for the 2001–2018 period.** Red pixels indicate
837 delays in $\text{EOS}_{10/50}$ dates (c, e), a longer duration of the senescence period (g), or increases in pre-solstice
838 GPP (a) or autumn temperature (i); blue pixels indicate advances in $\text{EOS}_{10/50}$, a shorter duration of the
839 senescence period, or decreases in pre-solstice GPP and autumn temperature. b, d, f, h, j, Trend means
840 and 95% confidence ranges summarized for each degree latitude. All trends were inferred from linear,
841 univariate models. k-m, Linear regression ($\pm 95\%$ confidence interval) between pixel-level temporal trends
842 in k) pre-solstice GPP and EOS_{10} dates, l) autumn temperature and EOS_{50} dates, and m) autumn
843 temperature and senescence duration. Areas with large increases in pre-solstice GPP also show larger
844 advances in EOS_{10} dates, whereas areas in which GPP has been declining tend to show delays in EOS_{10}
845 (k). Areas with large increases in autumn temperature show larger delays in EOS_{50} dates (l) and,
846 accordingly, a prolongation of senescence duration (m). Autumn temperature represents the mean day-time
847 autumn temperature for the autumn period that was most highly correlated with EOS_{50} dates (Autumn T_{day} ;
848 see *Autumn temperature intervals* in methods section).
849



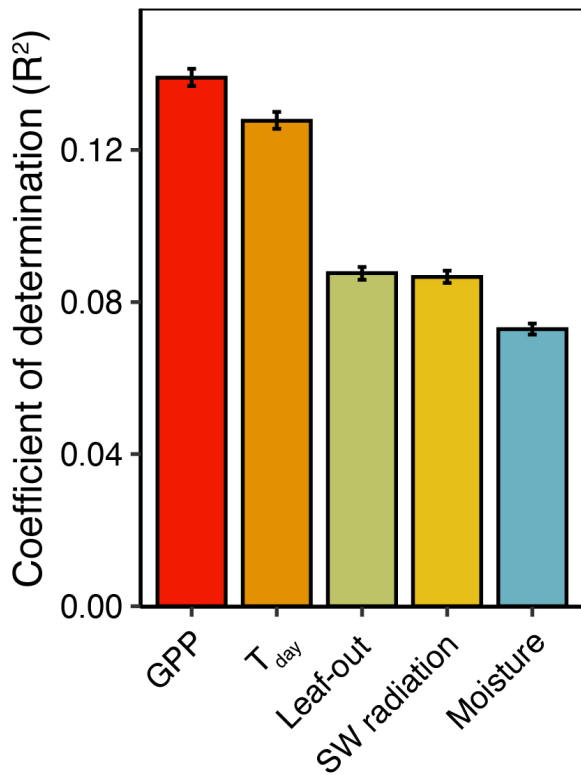
Extended Data Fig. 6. The effect of autumn temperature on EOS₁₀ (a) and EOS₅₀ dates (b,c).
 Standardized regression coefficients for the univariate correlations between autumn temperature intervals and EOS dates. Temperature intervals refer to the mean night-time (T_{night}) or day-time (T_{day}) temperatures for the periods 10 to 120 days before the mean EOS₁₀ or EOS₅₀ date at each time series. Models were run at the pixel-level (a, b) or individual-level (c) and the mean time series-level effects ($\pm 95\%$ confidence intervals) are shown separately for mixed, deciduous broadleaf, evergreen needleleaf, and deciduous needleleaf forests for the satellite-based analyses and for the four European species included in the PEP725 dataset.

850
 851
 852
 853
 854
 855
 856
 857
 858
 859
 860
 861

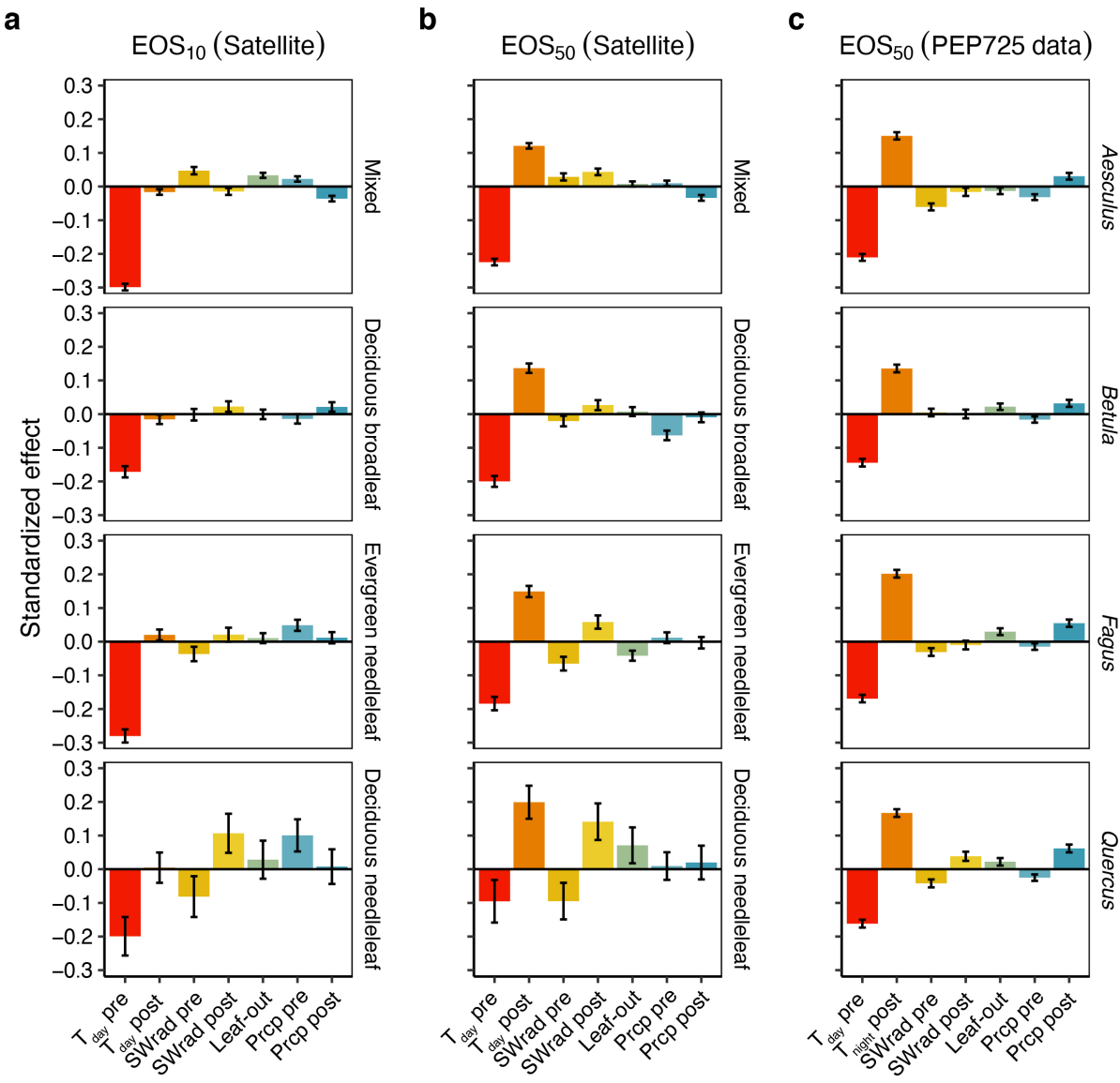


862
863
864
865
866
867
868
869
870

Extended Data Fig. 7. Moving-window analysis based on European long-term observations (PEP725 data), showing the average dates when trees became sensitive to autumn temperatures for each 20-year time period from 1966 to 2015 (a) and for each 15-year time period from 1981 to 2015 (b). Coloured lines indicate species-specific results, the black line represents the mean ($\pm 95\%$ confidence interval) across all species, the black dashed line indicates the trend from a linear model. This trend line shows that the start date of the temperature-sensitive autumn period advanced by 2.0 ± 0.7 days (mean $\pm 95\%$ confidence interval) per decade (a) or by 4.3 ± 0.9 days per decade for the 1981–2015 period (b).

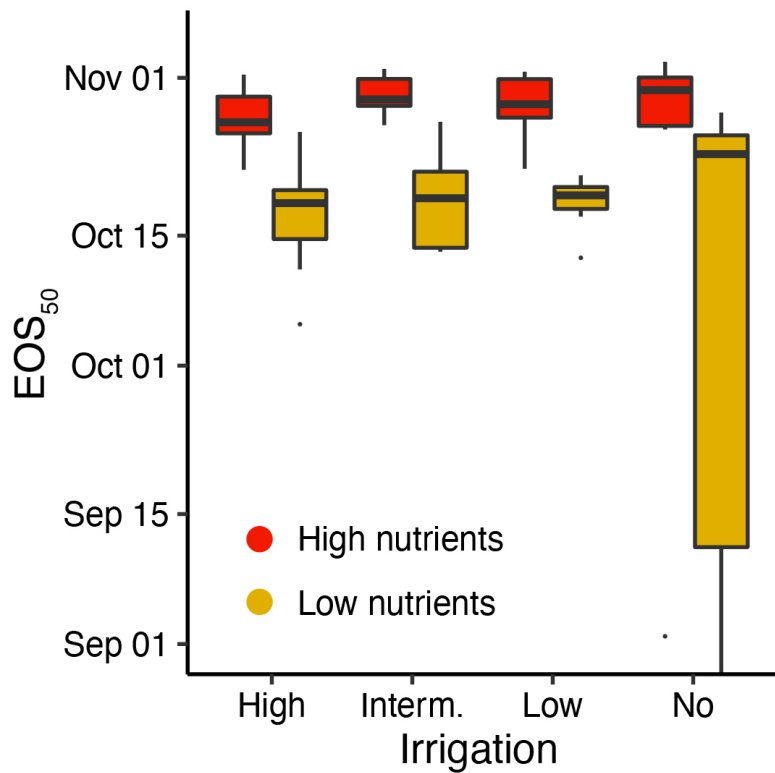


Extended Data Fig. 8. Coefficients of determination for the univariate effects of pre-solstice productivity (GPP), pre-solstice temperature, spring leaf-out dates, pre-solstice short-wave radiation, and pre-solstice soil moisture on the timing of senescence onset (EOS_{10}). For each variable, we ran univariate linear models, with GPP representing the cumulative productivity from leaf-out to June 21 (summer solstice), T_{day} , SW radiation, and moisture representing the average day-time temperature, short-wave radiation, or soil moisture from March 20 to June 21, and leaf-out representing the spring leaf-out date in the respective year. Models were run at the pixel-level and the mean coefficients of determination ($\pm 95\%$ confidence intervals) are shown.



884
885
886
887
888
889
890
891
892
893
894

Extended Data Fig. 9. The effects of pre- and post-solstice temperature, radiation, precipitation and spring leaf-out dates on inter-annual variation in the timing of EOS₁₀ (a) and EOS₅₀ (b, c) for each forest type (a,b) and tree species (c). We ran linear models including mean day-time temperature (T_{day}) and short-wave radiation (SWrad) and the sums of precipitation (prcp) from March 20 to June 21 (pre-solstice) and from June 22 to the mean EOS date of each time series (post-solstice) as well as spring leaf-out dates as predictor variables. Models were run at the pixel-level (a, b) or individual-level (c) and the mean effects ($\pm 95\%$ confidence intervals) are shown separately for mixed, deciduous broadleaf, evergreen needleleaf, and deciduous needleleaf forests for the satellite-based analyses and for the European species included in the PEP725 dataset. All variables were standardized to allow for effect size comparison.



Extended Data Fig. 10. Results of the nutrient and drought experiment. EOS₅₀ dates (day of 50% chlorophyll loss) for the eight treatment combinations, i.e., low and high soil nutrient status and no, low, intermediate and high irrigation. $P < 0.01$ for the nutrient treatment and $P = 0.17$ for the irrigation treatment.

895
896
897
898
899
900
901
902
903
904
905
906
907
908
909
910
911
912
913
914

Supplementary Files

This is a list of supplementary files associated with this preprint. Click to download.

- [ZohneretalSPSSupplement.pdf](#)